



Identification of typical diurnal patterns for clear-sky climatology of surface urban heat islands



Jiameng Lai^a, Wenfeng Zhan^{a,b,*}, Fan Huang^a, James Voogt^c, Benjamin Bechtel^d, Michael Allen^e, Shushi Peng^f, Falu Hong^a, Yongxue Liu^g, Peijun Du^{g,*}

^a Jiangsu Provincial Key Laboratory of Geographic Information Science and Technology, International Institute for Earth System Science, Nanjing University, Nanjing, Jiangsu 210023, China

^b Jiangsu Center for Collaborative Innovation in Geographical Information Resource Development and Application, Nanjing 210023, China

^c Department of Geography, University of Western Ontario, London N6A 5C2, ON, Canada

^d Center for Earth System Research and Sustainability, Universität Hamburg, 20146 Hamburg, Germany

^e Department of Geography, University of California, Santa Barbara, 1832 Ellison Hall, Santa Barbara, CA 93106, USA

^f Sino-French Institute for Earth System Science, College of Urban and Environmental Sciences, Peking University, Beijing 100871, China

^g Department of Geographic Information Science, Nanjing University, Nanjing, Jiangsu 210023, China

ARTICLE INFO

Keywords:

Surface urban heat island
Thermal remote sensing
Land surface temperature
Diurnal temperature cycle
MODIS product

ABSTRACT

Understanding the diurnal dynamics of surface urban heat islands (SUHIs) is an indispensable step towards their full interpretation at multiple time scales. However, because of the tradeoff between the spatial and temporal resolutions of satellite-derived land surface temperature (LST) data, the climatology, variety, and taxonomy of diurnal SUHI (DSUHI) patterns remain largely unknown for numerous cities with different bioclimates. By combining daily MODIS LST data with a newly developed four-parameter diurnal temperature cycle (DTC) model, we selected 354 Chinese megacities located in different bioclimatic zones to examine the characteristics of the DSUHI descriptors and systematically investigate the prevalent DSUHI temporal patterns.

The DSUHI variations demonstrate that both the daily maximum and minimum SUHI intensity (SUHII) can occur during most periods of the day, although these intensities are more likely to occur in the early morning and noon/afternoon. Our results also reveal that both strong SUHIs (SUHII > 3 K) and surface urban cool islands (SUCIs) (SUHII < 0 K) are more prevalent than those identified directly through the four MODIS transits. According to the SUHI dynamics, five typical DSUHI temporal patterns are identified: standard-spoon, weak-spoon, quasi-spoon, inverse-spoon, and straight-line patterns. A gradient was found with spoon-like patterns (DSUHI dynamics typically with a daytime valley and a roughly constant trend or a small peak at night) in North China and inverse-spoon (DSUHI dynamics with a typical daytime peak and a constant trend at night) or straight-line patterns (DSUHI dynamics virtually unchanged all day) in South China. The DSUHI shapes were found to be greatly controlled by the urban-rural contrast in the normalized difference vegetation index (NDVI) and urban geometry. Our results not only advance our understanding of the diurnal climatology of SUHIs but also provide a basis for urban surface heat mitigation by identifying the possible timing of the mitigation requirement.

1. Introduction

The rapid urbanization of the past few decades has continuously

converted natural habitats into urban surfaces and it has also had a large impact on the urban climate, environment and ecology (Kalnay and Cai, 2003). One of the most distinctive urbanization-induced

Abbreviations: CUHI, canopy layer urban heat island; CUHII, canopy layer urban heat island intensity; DCUHI, diurnal canopy layer urban heat island; DSUHI, diurnal surface urban heat island; DTC, diurnal temperature cycle; GST, ground surface temperature; LST, land surface temperature; NDVI, normalized difference vegetation index; SAT, surface air temperature; SUCI, surface urban cool island; SUHI, surface urban heat island; SUHII, surface urban heat island intensity; UHI, urban heat island

* Corresponding authors at: Nanjing University at Xianlin Campus, No.163 Xianlin Avenue, Qixia District, Nanjing, Jiangsu 210023, China.

E-mail addresses: mg1727056@mail.nju.edu.cn (J. Lai), zhanwenfeng@nju.edu.cn (W. Zhan), nju_huangfan@163.com (F. Huang), javoogt@uwo.ca (J. Voogt), benjamin.bechtel@uni-hamburg.de (B. Bechtel), m_allen@umail.ucsb.edu (M. Allen), speng@pku.edu.cn (S. Peng), hongfalu@foxmail.com (F. Hong), yongxue@nju.edu.cn (Y. Liu), dupjrs@gmail.com (P. Du).

<https://doi.org/10.1016/j.rse.2018.08.021>

Received 17 February 2018; Received in revised form 3 July 2018; Accepted 16 August 2018

Available online 21 August 2018

0034-4257/© 2018 Elsevier Inc. All rights reserved.

outcomes is the urban heat island (UHI), a phenomenon in which urban temperatures tend to be higher than that of the surrounding area (Oke, 1982). The UHI has been reported in numerous cities worldwide (Stewart and Oke, 2012) and it profoundly affects people's lives (Akbari and Konopacki, 2005; Gong et al., 2012; Patz et al., 2005). Typically, the UHI denotes the elevated urban temperatures measured in the canopy layer and/or at the skin-surface. They are referred to as the canopy layer UHI (CUHI) and the surface UHI (SUHI), respectively, both of which have been documented extensively (Clinton and Gong, 2013; Flores et al., 2016; Hu and Brunsell, 2015; Nichol, 2005; Oke, 1982; Pichierri et al., 2012; Stewart and Oke, 2012; Wang et al., 2017).

The CUHI and SUHI have dissimilar temporal patterns on different time scales, and the exploration of these different patterns has been a major focus of previous UHI studies (Anniballe et al., 2014; Lazzarini et al., 2013; Wang et al., 2017). CUHI dynamics from very small (e.g., hourly) to very large (e.g., inter-annual) time scales can be observed directly through high-frequency in-situ surface air temperature (SAT) measurements (Chow and Roth, 2006; de Faria Peres et al., 2018; Ren et al., 2007; Runnalls and Oke, 2000). Similarly, high-frequency in-situ ground surface temperatures (GSTs) can be used to characterize the multi-temporal development of the SUHI (Wang et al., 2017). Nevertheless, GSTs obtained from stations, when compared with in-situ SATs, are highly sensitive to the local surface type and are therefore characterized by a high spatial heterogeneity, making such point-based GSTs far less capable of representing the overall thermal differences between urban and nonurban areas. Satellite-derived land surface temperatures (LSTs) overcome this shortcoming by providing spatially continuous data of the surface thermal status at a large scale (Voogt and Oke, 2003; Weng, 2009), and such data have been widely used in SUHI investigations under clear-sky conditions (e.g., Li et al., 2012; Imhoff et al., 2010; Keramitsoglou et al., 2011; Meng et al., 2018; Quan et al., 2014; Schwarz et al., 2011; Shen et al., 2016; Stathopoulou and Cartalis, 2009; Zhou et al., 2014).

Consequently, investigations of SUHI temporal variations on seasonal/monthly and inner-annual timescales have benefited greatly from the accumulation of thermal remote sensing data, particularly those from polar-orbiting satellites with relatively fine spatial resolutions (i.e., Landsat/TM, ETM+, and TIRS, NOAA/AVHRR, Terra & Aqua/MODIS, along with others) (Bechtel, 2015; Clinton and Gong, 2013; Streutker, 2003; Tran et al., 2006; Zhou B. et al., 2013). Polar-orbiting satellites, however, only sample LSTs at a comparatively low frequency (only two to four times per day at most) primarily because of the trade-off between the spatial and temporal resolution of satellite observations (Sobrino et al., 2012; Zhan et al., 2013). This temporal discontinuity in the LST records from polar orbiting satellites limits SUHI studies to discrete times during a diurnal cycle when the satellite transits (Clinton and Gong, 2013; Nichol and To, 2012; Peng et al., 2012; Shastri et al., 2017), while the true and continuous SUHI temporal pattern during a diurnal cycle (hereafter termed the DSUHI temporal pattern) has been less investigated.

To better understand true DSUHI temporal patterns, two strategies have been devised. The first uses spatially downscaled high-frequency LSTs obtained from geostationary satellites (e.g., the GOES satellite operated by the National Oceanic and Atmospheric Administration, the FY satellite by the China Meteorological Administration and the MSG satellite by the European Organization for the Exploitation of Meteorological Satellites). This approach is termed the *spatial downscaling strategy*. It can generate hourly or sub-hourly LST data with a spatial resolution of 1 km or finer, which are suitable for DSUHI investigations (Bechtel et al., 2012; Sismanidis et al., 2015a, b; Zakšek and Oštir, 2012; Zhou J. et al., 2013). The other strategy combines LST observations from polar-orbiting satellites and the diurnal temperature cycle (DTC) models (hereafter termed the *DTC modeling strategy*) to reconstruct temporally continuous LST dynamics, from which DSUHI temporal patterns can be explored (Fang et al., 2017).

Using these two strategies, DSUHI temporal patterns have been

investigated in a very limited number of case cities, and they appear to exhibit a greater variety than diurnal CUHI (DCUHI) patterns. Specifically, the DCUHI usually exhibits a higher intensity at nighttime compared to daytime (Oke, 1982), while the DSUHI exhibits no general patterns but rather varies among different cities/seasons. For example, on typical days in spring, autumn, and winter in Beijing, as well as for summer in Athens, studies have reported that DSUHI and DCUHI patterns are similar (Sismanidis et al., 2015b; Zhou et al., 2013a). The CUHI and SUHI intensities (CUHIs and SUHIs) in these two cities generally decrease after sunrise, reach a minimum around solar noon, and then increase until the evening, after which stable and significant nighttime SUHIs (SUHIs) persist until the following sunrise. The summer seasons of some other cities (Rome, Beijing, and most of the cities in China within the Yangtze River Delta urban agglomeration) exhibit a different DSUHI temporal pattern: The SUHIs after sunrise increase quickly, generally reach a peak within 2 h after the solar noon, and then decrease until sunset and remain relatively constant throughout the night (Fang et al., 2017; Sismanidis et al., 2015b; Zhou et al., 2013a). Yet another DSUHI temporal pattern was found for typical summer days in Paris and Istanbul: The SUHIs first exhibit a four-hour downward trend after sunrise; they then increase to a diurnal maximum mostly in the afternoon, followed by a slow downward trend until sunset, and a quasi-stationary trend until the next sunrise (Sismanidis et al., 2015b; Zakšek and Oštir, 2012).

DSUHI temporal patterns have been recognized preliminarily using the *spatial downscaling* and *DTC modeling* strategies as summarized above; however, we have identified two issues requiring further investigation. First, previously acknowledged DSUHI temporal patterns were mostly obtained on a single or few days across a yearly cycle, and thus the climatological DSUHI temporal patterns remain largely unknown. Second, previous reports of DSUHI temporal patterns focused on a single or few cities located in a small number of bioclimatic zones; such case studies are unable to provide a full insight into the DSUHI temporal patterns that exhibit great variations among different cities. Therefore, our current understanding of the variety and taxonomy of the prevalent DSUHI temporal patterns for numerous cities with very different bioclimates on a large (e.g., continental) scale remains preliminary.

To address these limitations and derive a full understanding of the true diurnal dynamics of the large-scale climatological SUHI, in the present study we selected > 300 cities within different bioclimatic zones across China. By incorporating a newly developed four-parameter DTC model, the *DTC modeling* strategy was used for deriving the temporally continuous DSUHI dynamics. We choose *DTC modeling* over the *spatial downscaling* strategy because of the advantages of the former strategy in terms of its data and the convenience in its methodology (further explanations are given in Section 3.2). The characteristic descriptors and the prevalent patterns of the DSUHI were investigated over the full annual cycle of months/seasons from the climatological perspective. This study provides a simple yet efficient methodology for studying DSUHI temporal patterns. The identified DSUHI temporal patterns deliver, to the best of our knowledge, a first insight into the taxonomy of the SUHI diurnal dynamics, as well as how DSUHI temporal patterns may vary among different bioclimatic zones. These provide for an improved interpretation of the SUHI on multiple spatiotemporal scales.

2. Study area

The past three to four decades have witnessed a very rapid urbanization of cities in China, wherein significant UHIs have been reported (Wang et al., 2015; Zhou et al., 2014). In this study, we chose 354 megacities with urban areas exceeding 10 km^2 (the delineation of urban areas is given in Section 3.2.3) as the study area (Fig. 1). These cities are mostly distributed in seven bioclimatic zones according to Zheng et al. (2010): Southern Subtropical (SS), Mid Subtropical (MS),

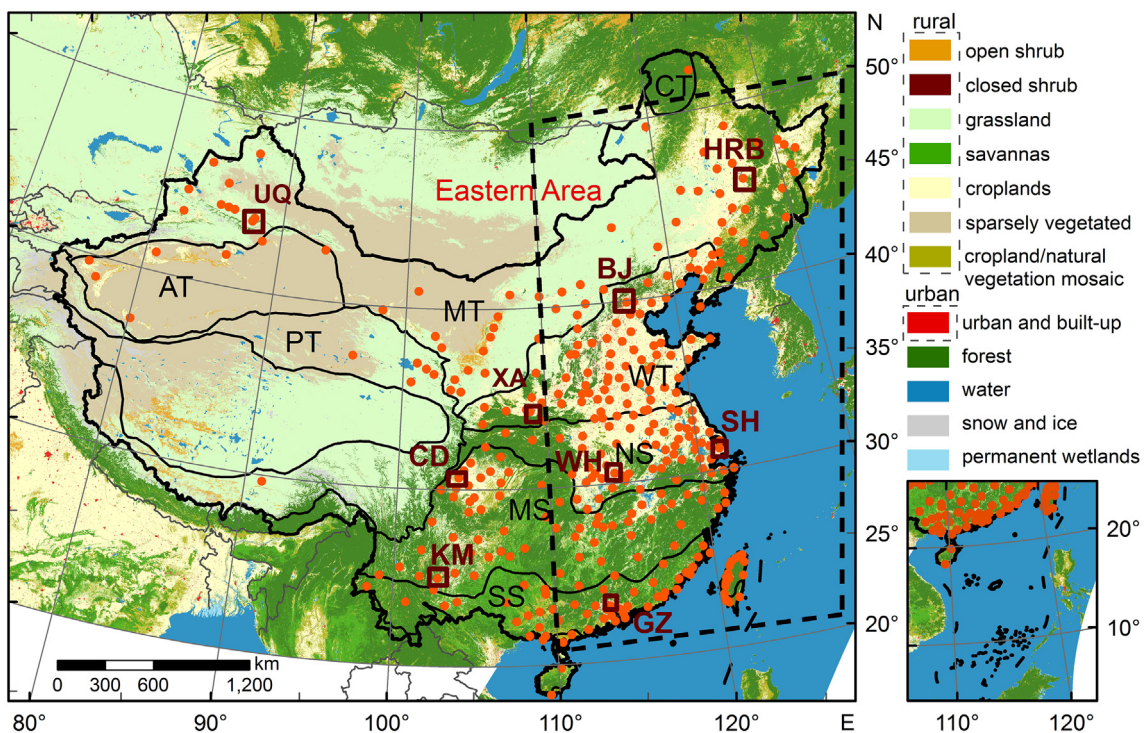


Fig. 1. Geolocation of the selected 354 cities and climate zones across China. The climate zones are Southern Subtropical (SS), Mid Subtropical (MS), Northern Subtropical (NS), Warm Temperate (WT), Mid Temperate (MT), Plateau Temperate (PT), Arid Temperate (AT), and Cold Temperate (CT). The nine selected megacities are Harbin (HRB), Urumqi (UQ), Beijing (BJ), Xi'an (XA), Shanghai (SH), Wuhan (WH), Chengdu (CD), Kunming (KM), and Guangzhou (GZ).

Northern Subtropical (NS), Warm Temperate (WT), Mid Temperate (MT), Plateau Temperate (PT), and Arid Temperate (AT), from southeast to northwest. For these climate zones, temperature and precipitation generally decrease from south to north. Note that there exists an extra Cold Temperate (CT) zone in northernmost China, but the Cold Temperate zone was not considered in this study because it contains only a single city.

For further analysis, we paid closer attention to eastern cities (245 cities in total with longitudes $> 110^{\circ}$ E; see the diamond-shaped area in Fig. 1), which are in areas of low terrain with elevations generally lower than 500 m, to analyze the latitudinal variation of the DSUHI by controlling the effects from city topography. The associated results are provided in the Supplementary Information. We further selected nine megacities (Fig. 1) for comparison of the satellite-derived DSUHI with DCUHI patterns. These megacities, from north to south, include Harbin, Urumqi, Beijing, Xi'an, Shanghai, Wuhan, Chengdu, Kunming, and Guangzhou, with the associated results also given in Supplementary Information.

3. Data and methods

3.1. Data

3.1.1. MODIS products

The land cover, LST, and normalized difference vegetation index (NDVI) products provided by MODIS were used in this study. The land cover data were derived from the annual MCD12Q1 product (collection 5, the spatial resolution is 500 m) acquired by the Terra and Aqua satellites in 2012. In total, 17 land cover types were identified under the International Geosphere-Biosphere Program (IGBP) classification scheme. The LST data were obtained from the MOD11A1 and MYD11A1 products (collection 6, acquired by the Terra and Aqua satellites, respectively), with a spatial resolution of 1 km. All the LST images acquired from 2012 to 2016 were used. They include 160,776 tiles of LST images in total ($4 \text{ transits/day} \times 22 \text{ tiles}$ over

1827 day). The generalized split-window LST algorithm is used for the generation of MODIS LSTs (Wan and Dozier, 1996) and the associated retrieval errors are $< 1.0 \text{ K}$ in most cases (Wan, 2008). To suppress impacts from abnormal retrieved LST values, pixels with LST values $> 12.0 \text{ K}$ larger/smaller than their neighbors in the same row were excluded (Gawuc and Struzewska, 2016; Lai et al., 2018). To obtain a climatic representation of SUHIs, the daily LST products were further aggregated into monthly and seasonal composites, during which only clear-sky data were used. The NDVI data were derived from the monthly MOD13A3 and the MYD13A3 products (collection 6, acquired by the Terra and Aqua satellites, respectively) from 2012 to 2016, with a spatial resolution of 1 km. In total they include 2640 tiles of NDVI images ($2 \text{ transits/month} \times 22 \text{ tiles} \times 12 \text{ months/year} \times 5 \text{ years}$).

3.1.2. FY geostationary satellite data

Geostationary LST data from the Visible Infrared Spin Scan Radiometer (VISSR) onboard the FY-2F satellite were used to provide DSUHI temporal patterns for comparison with those derived from MODIS data. The FY-2F LST data were retrieved using a split-window algorithm (Tang et al., 2008), and there is no quality flag available. This study employed all of the hourly FY-2F LST data (with a spatial resolution of 5 km) in 2016. A seasonal composition procedure was conducted based on all the clear-sky data with the purposes of reducing the impacts from data gaps caused by cloud contamination and deriving DSUHI temporal patterns from a climatological perspective.

3.1.3. In-situ SATs and GSTs

To conduct a comparison between the LST-based DSUHI, GST-based DSUHI and SAT-based DCUHI, we used the hourly SAT and GST data obtained from ground-based weather stations in the nine selected megacities (refer to Fig. 1 for their locations and Supplementary information for the results). The stations were flagged as urban or rural sites according to their latitudes and longitudes available in the dataset, as well as by the delineation of urban areas and rural backgrounds as defined in Section 3.2.3. The numbers of urban and rural stations for

Table 1

Numbers of weather stations for the nine selected megacities.

City name	Climate zone	Urban site num.	Rural site num.
Harbin	Mid Temperate	7	83
Urumqi	Mid Temperate	5	39
Beijing	Warm Temperate	65	211
Xi'an	Warm Temperate	20	82
Shanghai	Northern Subtropical	20	41
Wuhan	Northern Subtropical	17	71
Chengdu	Mid Subtropical	35	161
Kunming	Mid Subtropical	20	110
Guangzhou	Southern Subtropical	46	94

these nine megacities are listed in [Table 1](#). The SATs and GSTs were obtained from automatic weather station (AWS) systems fixed at 1.5 m above ground and at the ground surface. Two types of AWS system were used, including Vaisala MAWS301 and CAWS600, and the corresponding data accuracy is ± 0.3 °C at 20 °C ([Wang et al., 2017](#)).

3.2. Methodology

As explained in [Section 1](#), it is difficult to directly derive the true DSUHI temporal patterns through satellite-derived LST products. Strategies that can enhance the spatiotemporal resolution of LST data are therefore needed. This study used the *DTC modeling* strategy mainly for its advantages in the following two aspects. First, polar-orbiting satellite sensors (e.g., MODIS) are able to provide mature and globally consistent LST products. Moreover, the SUHIs derived from MODIS data are anticipated to suffer less from surface thermal anisotropy once a temporal composition is created by averaging all valid LSTs obtained from multiple viewing angles. Second, the *DTC modeling* strategy is easy to implement so that the computational complexity is greatly decreased, especially when applied over a large number of cities. The advantages in terms of satellite data and convenience in terms of algorithm implementation make the *DTC modeling* strategy applicable to hundreds of cities across extensive surfaces. We nevertheless acknowledge that limitations also exist with the *DTC modeling* approach; a discussion of these limitations is provided in [Section 4.4.1](#).

3.2.1. Adjusted GOT09 (termed GOT09_A) model with four controlling parameters

DTC models are essential for acquiring true DSUHI temporal patterns with temporally sporadic LSTs during a diurnal cycle. Most of the previous DTC models have 5–6 parameters, which exceed the four daily transits of the bi-polar-orbiting satellites (e.g., MODIS and AVHRR), and therefore, they cannot be used to simulate diurnal LST dynamics based on these satellite data ([Huang et al., 2014](#)). Instead, DTC models with only four controlling parameters (hereafter termed four-parameter DTC models) are required. Several parameterization schemes have been proposed to reduce the number of parameters of the present DTC models to four. [Hong et al. \(2018\)](#) recently compared ten four-parameter DTC models derived from different parameterization schemes and most of the frequently used DTC models. A comprehensive assessment revealed that the GOT09_A model, which was modified from the GOT09 model developed by [Götsche and Olesen \(2009\)](#), had the highest accuracy among the ten four-parameter DTC models, mainly in three respects. First, the root-mean-square error of the GOT09_A model is approximately 1.2 K, which is the lowest among the investigated four-parameter DTC models. Second, the variability of its accuracy is the lowest over different surface types, indicating the least amount of fluctuations produced by differences in surface thermal status. Third, compared with other four-parameter DTC models, this model exhibits the most stable performance over different daily periods, especially for the period shortly after sunrise; and the prediction accuracy of this period can greatly determine the daily mean accuracy.

We employed the GOT09_A model to simulate the LST diurnal dynamics for its clarified highest performance among the existing four-parameter DTC models. The general formula of its original six-parameter DTC model, i.e., the GOT09 model, is written as follows ([Götsche and Olesen, 2009](#)):

$$T(t) = \begin{cases} T_0 + T_a \cdot \frac{\cos(\theta_z)}{\cos(\theta_{z,\min})} \cdot \exp[\tau \cdot (m_{\min} - m(\theta_z))], & t < t_s \\ T_0 + \delta T + \left[T_a \cdot \frac{\cos(\theta_{zs})}{\cos(\theta_{z,\min})} \cdot \exp[\tau \cdot (m_{\min} - m(\theta_{zs}))] - \delta T \right] \\ \cdot \exp\left[-\frac{12}{\pi k}(\theta - \theta_s)\right], & t \geq t_s \end{cases} \quad (1)$$

where $T(t)$ is the modeled LST at time t ; T_0 , T_a , t_m , t_s , δT and τ are the six controlling parameters, where T_0 represents the residual temperature, which is close to the sunrise temperature, T_a represents the daily temperature amplitude (i.e., the difference between the diurnally maximum and minimum temperatures), t_m and t_s represent the times when LST reaches its maxima and when LST attenuation begins (i.e., the start time of the exponential part of the DTC function), respectively, δT is the day-to-day temperature difference calculated as $T_0 - T(t)$ when t approaches ∞ , and τ is the total optical thickness (TOT); θ is the thermal hour angle relative to the thermal noon at time t_m ([Götsche and Olesen, 2009](#)); θ_z is the solar zenith angle corresponding to θ ; $\theta_{z,\min}$ is the minimum zenith angle at time t_m ; θ_s and θ_{zs} correspond to θ and θ_z at time t_s ; $m(\theta_z)$, m_{\min} , and $m(\theta_{zs})$ are the relative air masses at θ_z , $\theta_{z,\min}$, and θ_{zs} , respectively; k is the attenuation constant of the LST. All these parameters, apart from the six controlling parameters, can be calculated according to the local latitude, longitude, and day of year ([Götsche and Olesen, 2009](#)).

Two parameter reduction strategies were employed to reduce the six parameters of the GOT09 model to four parameters, therefore formulating an adjusted model called GOT09_A. The first strategy is to fix δT to zero, which is plausible because δT usually fluctuates around zero ([Schädlitz et al., 2001](#)). The second strategy is to fix the TOT (τ) to a constant value of 0.01, which has been determined to be generally the best option for all types of surfaces in different climate zones ([Hong et al., 2018](#)). These two parameter reduction strategies are even more reasonable for the present study because the monthly/seasonal composites of the daily LSTs were used for each transit time. For example, the day-to-day temperature difference (δT) would be statistically equal to zero as synoptic conditions can be suppressed for monthly composites of LSTs. The ultimate formula for GOT09_A can be written as follows, as shown by [Hong et al. \(2018\)](#):

$$T(t) = \begin{cases} T_0 + T_a \cdot \frac{\cos(\theta_z)}{\cos(\theta_{z,\min})} \cdot \exp[0.01 \times (m_{\min} - m(\theta_z))], & t < t_s \\ T_0 + T_a \cdot \frac{\cos(\theta_{zs})}{\cos(\theta_{z,\min})} \cdot \exp[0.01 \times (m_{\min} - m(\theta_{zs}))] \\ \cdot \exp\left[-\frac{12}{\pi k}(\theta - \theta_s)\right], & t \geq t_s \end{cases} \quad (2)$$

where only four controlling parameters (T_0 , T_a , t_m , and t_s) exist.

3.2.2. Derivation of DSUHI temporal patterns using MODIS data

3.2.2.1. Delineation of urban and rural areas. The delineation of urban and rural areas was based on the MODIS land cover product MCD12Q1 (see [Section 3.1.1](#)). The pixels classified as snow and ice were first excluded due to their extremely low temperatures. The pixels classified as water and permanent wetlands were also removed to eliminate the impacts of water bodies. Forests were also excluded because they are primarily distributed on undulating mountains and may consequently be inappropriate to be used as rural backgrounds – the LSTs over mountain forests are considerably lower than those over urban and suburban areas. Within each city, the pixels with elevations exceeding ± 50 m of the median elevation of the built-up pixels were

also removed based on the Global 30 Arc-Second Elevation (GTOPO30) data, to suppress the impacts from elevation on temperatures. The median rather than the mean elevation was used here to eliminate fragmentary built-up pixels with extremely high or low elevations. Among the remaining pixels within the administrative border of each city (the administrative borders were obtained from the National Geomatics Center of China), those classified as built-up were flagged as urban areas, while the remaining pixels were referred to as rural areas (Schwarz et al., 2011; Zhou et al., 2010). Note that here we chose the administrative borders rather than the buffer zone to delineate the rural areas, mainly considering that: (1) it remains difficult to simply adopt a buffer radius for all the cities with different sizes, especially when there exists no common standard for the radius definition of rural buffers; and (2) for Chinese cities, the rural areas within the administrative boundaries typically correspond well to the associated urban sizes. Finally, the delineated urban and rural images were resampled to 1 km to bridge their scale difference with the LST/NDVI products using the nearest neighbor strategy.

3.2.2.2. Calculation of DSUHI temporal patterns. We used SUHII, which is a widely used indicator in SUHI studies (Voogt and Oke, 2003), to quantify the magnitude of the SUHI effects. The SUHII is usually calculated as the difference between the mean urban and rural LSTs (Imhoff et al., 2010). To derive the DSUHI temporal patterns from the original four daily MODIS observations, the diurnal LST dynamics need to be simulated first using the aforementioned GOT09_A model. For each urban and rural pixel, the four thermal observation inputs required by the GOT09_A model were computed through monthly/seasonal temporal aggregations of the corresponding daily MODIS transits to obtain clear-sky climatological DSUHI temporal patterns, rather than those on a single day, which are impacted by specific synoptic and soil conditions. Thus, we were able to acquire four valid thermal observations within a climatological diurnal cycle with minimal influence from cloud cover: $[t_1, T(t_1)]$, $[t_2, T(t_2)]$, $[t_3, T(t_3)]$, and $[t_4, T(t_4)]$, where t_1 , t_2 , t_3 , and t_4 are the temporally averaged acquisition times, and $T(t_1)$, $T(t_2)$, $T(t_3)$, and $T(t_4)$ are the associated composites of LSTs. Based on these four thermal observation inputs, the four controlling parameters of the GOT09_A model, including T_0 , T_a , t_m , and t_s , were computed using the Levenberg-Marquardt curve fitting algorithm provided by Matlab 2015a for each pixel. The temporally continuous SUHII were finally estimated by the following formula:

$$I(t) = T_{\text{urban}}(t) - T_{\text{rural}}(t) \quad (3)$$

where $I(t)$ is the SUHII at time t within a climatological diurnal cycle, and $T_{\text{urban}}(t)$ and $T_{\text{rural}}(t)$ are the mean temperatures for all urban and rural pixels at time t , respectively.

3.2.2.3. Descriptors used to represent DSUHI temporal patterns. Descriptors that characterize the major diurnal features are needed to represent and then differentiate DSUHI temporal patterns. We chose six descriptors to quantitatively characterize the DSUHI variations: (1) the daily maximum SUHII (termed I_{\max}), (2) the time when the maximum SUHII occurs (termed t_{\max}), (3) the duration of strong SUHI ($\text{SUHII} > 3 \text{ K}$) within a daily cycle, (4) the daily minimum SUHII (termed I_{\min}), (5) the time when the minimum SUHII appears (termed t_{\min}), and (6) the duration of the surface urban cold island (SUCI) within a daily cycle. A strong SUHI in this study is referred to as the status when the SUHII exceeds 3.0 K because most global megacities have an annual SUHII less than this intensity (Peng et al., 2012); and the SUCI is defined as the occurrence of a negative SUHII (i.e., the SUHII is less than zero). Note that it is impossible to calculate these six descriptors directly based on the four daily MODIS LST acquisitions without the diurnal modeling process.

3.2.2.4. Identification of typical DSUHI temporal patterns. Considering that SUHI variations were largely impacted by bioclimatic conditions

(Zhao et al., 2014), we further investigated the variations of DSUHI temporal patterns depending on bioclimatic zones. To achieve the identification and taxonomy of the prevalent DSUHI temporal patterns, the derived temporally continuous DSUHI variations were firstly averaged among all the cities within each bioclimatic zone. The DSUHI variations were then classified into typical patterns mostly according to the following criteria: (1) the diurnal variations of the change rate of the DSUHI intensity ($\Delta I/\Delta t$), (2) the appearance time of the I_{\max} and I_{\min} , and (3) the appearance of the SUCI. By these criteria, five typical patterns were finally identified. Note that more explanations on the classification criteria, as well as the associated characteristics and the possible mechanisms of these typical patterns will be provided in Section 4.2.

3.2.3. Analysis of the impact of NDVI on DSUHI temporal patterns

Previous reports have illustrated that the urban-rural contrast in NDVI (termed ΔNDVI) can explain a great portion of the daytime SUHII (Weng et al., 2011; Yuan and Bauer, 2007) and that the NDVI is closely related to the diurnal LST dynamics (Duan et al., 2014; Jin and Dickinson, 1999). We, therefore, speculated that vegetation status could be one of the dominant controls of DSUHI temporal patterns. To test this hypothesis, we used the Beijing metropolis as an example to illustrate the ΔNDVI controls on the DSUHI temporal patterns. To elaborately investigate the possible variations in the DSUHI temporal patterns under different ΔNDVI values, we calculated the DSUHI temporal patterns based on selected urban and rural pixels with specific categories of NDVI values rather than based on the entire set of urban and rural pixels. In particular, the urban pixels were divided into five categories with NDVI values of 0.0–0.2, 0.2–0.4, 0.4–0.6, 0.6–0.8, and 0.8–1.0. The rural pixels were divided into four categories with NDVI values of 0.2–0.4, 0.4–0.6, 0.6–0.8, and 0.8–1.0 (no rural pixels have NDVI values < 0.2). The DSUHI temporal patterns were computed based on different combinations of these five categories of urban pixels and four categories of rural pixels, and the variability of the DSUHI temporal patterns that were governed by different ΔNDVI values was finally identified. The detailed results related to this issue are presented in Section 4.3.

3.2.4. Derivation of the DSUHI temporal patterns using FY-2F LSTs

The derivation of the DSUHI temporal patterns using FY-2F and MODIS data is similar. Three steps are involved: First, the hourly FY-2F LSTs were seasonally aggregated into 24 climatological thermal observations, i.e., $[t_1, T_1]$, $[t_2, T_2]$, ..., $[t_{24}, T_{24}]$, where t_1 to t_{24} denote the acquisition time and T_1 to T_{24} denote the composited LST value at the corresponding time. Second, the 24 LSTs were employed as the input data for the DTC model to fit the four controlling parameters. Finally, the hourly DSUHI intensity (DSUHII) was estimated using Eq. (3). A DTC model was used in this study to decrease the uncertainty of the FY-2F LST product, which can sometimes be substantial because no quality control was conducted for this product and abnormal LST values occasionally occur even after a seasonal composition process.

3.2.5. Derivation of the hourly variations of CUHII and SUHII with in-situ SATs and GSTs

The SAT-based DCUHI and GST-based DSUHI variations were computed using the hourly in-situ SAT and GST data with the following formula:

$$I_{\text{site}}(t) = T_{\text{site_urban}}(t) - T_{\text{site_rural}}(t) \quad (4)$$

where $I_{\text{site}}(t)$ is the hourly UHI intensity calculated by the in-situ SATs or GSTs; and $T_{\text{site_urban}}(t)$ and $T_{\text{site_rural}}(t)$ are the mean in-situ temperatures for all the urban and rural stations at the corresponding time t , respectively.

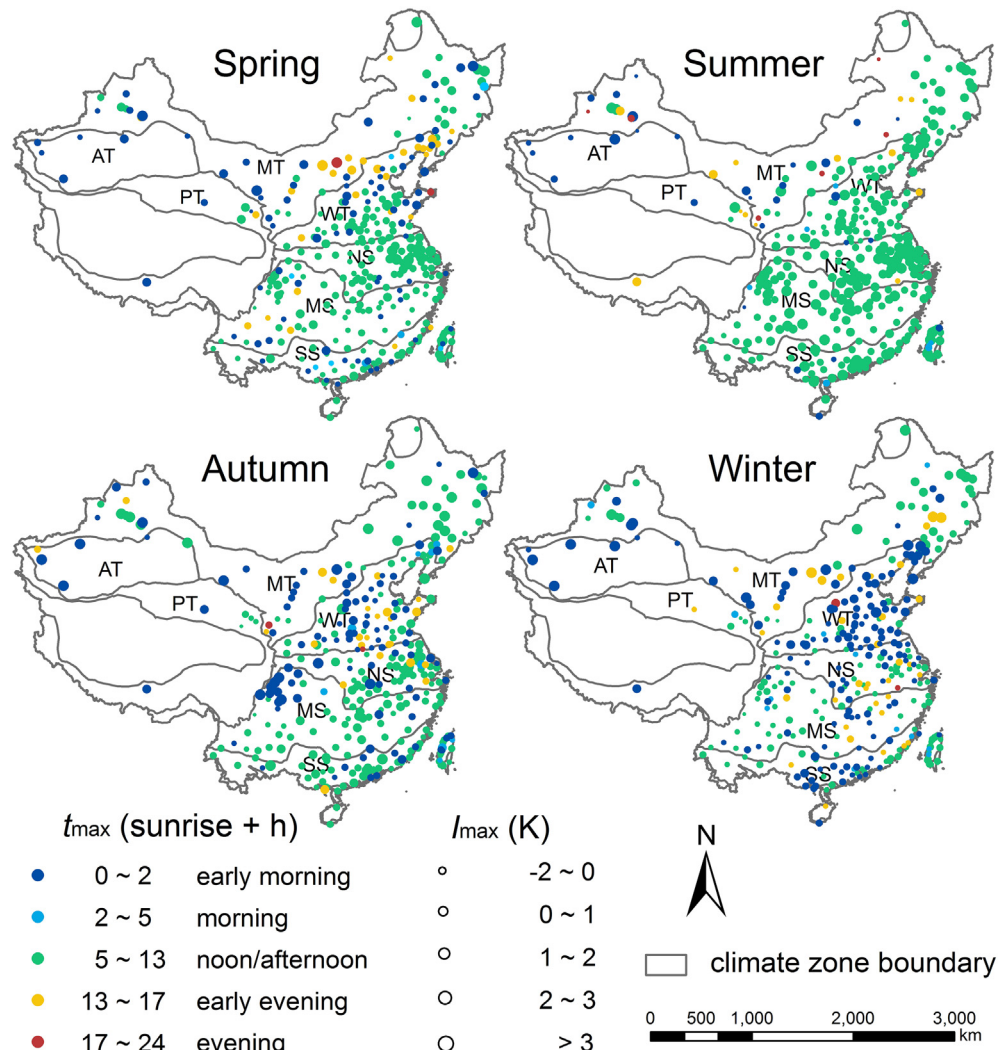


Fig. 2. Maximum SUHII (I_{\max}) and the corresponding associated occurrence time (t_{\max}) for all the cities. The dot color indicates the period within which t_{\max} occurs while the size represents the I_{\max} value. Spring, summer, autumn and winter are defined as: March–May, June–August, September–November and December–February, respectively. (For interpretation of the references to color in this figure legend, the reader is referred to the web version of this article.)

4. Results and discussion

4.1. Spatiotemporal variations of DSUHI descriptors

4.1.1. Daily maximum SUHII

The daily maximum SUHII (I_{\max}) for the four seasons and the corresponding occurrence times (t_{\max}) across all cities are displayed in Fig. 2. Note that t_{\max} herein is defined as the number of hours after sunrise rather than as the absolute local solar time; this is because the sunrise time, which differs for cities at different latitudes or in different seasons, directly determines the LST dynamics and therefore the DSUHI temporal patterns. The results show that I_{\max} has no fixed occurrence time. It occurs in totally different periods within a diurnal cycle in different seasons/cities, although it may occur more often in certain periods.

In general, t_{\max} occurs most frequently in noon/afternoon and early morning (Figs. 2 and 3). For $> 35\%$ (60%) of the cities in winter (spring, summer and autumn), t_{\max} is at noon or in the afternoon (5 to 13 h after sunrise); and for the early morning (within 2 h after sunrise), the proportion is $> 20\%$ in spring and autumn, $> 40\%$ in the winter, and 9% in summer. Fewer cities ($< 10\%$ in each season) have t_{\max} in the early evening (13 to 17 h after sunrise). By comparison, t_{\max} rarely occurs in the morning (2 to 5 h after sunrise) and especially in the

evening (17 h after sunrise). In each season, no $> 5\%$ of the cities have t_{\max} in the morning, and the corresponding percentages are $< 2\%$ for the evening. This accords with the usually more significant SUHII observed during the daytime (Tran et al., 2006; Peng et al., 2012).

The frequency distributions of t_{\max} (see Fig. 3) indicate that, among the four daily MODIS overpasses, the Aqua-day transit has the greatest probability of capturing I_{\max} , while the Aqua-night transit has the lowest probability. Moreover, for 67% (in the spring), 71% (summer), 58% (autumn), and 71% (winter) of the cities, none of the four transits is capable of capturing I_{\max} , which will typically result in an underestimation of I_{\max} if directly calculated from MODIS LST data. Note that uncertainties may occur for these two DSUHI descriptors related to the daily maximum SUHII (t_{\max} in particular) using the DTC approach, especially for the cities where I_{\max} is near sunrise. A detailed discussion of this issue is given in Section 4.4.1.

Based on the DTC approach, mean values (\pm standard deviations) of I_{\max} for all those cities are $1.4 (\pm 0.9)$, $2.0 (\pm 1.1)$, $1.2 (\pm 0.7)$, and $1.2 (\pm 1.0)$ K for spring, summer, autumn and winter, respectively. These small seasonal variations in I_{\max} , when compared with the variations obtained in some individual cities such as Berlin and Paris (Bechtel and Sismanidis, 2018), may be attributable to the averaging processes along the temporal scale (seasonal mean rather daily) as well as among cities within different bioclimatic zones. Despite the small

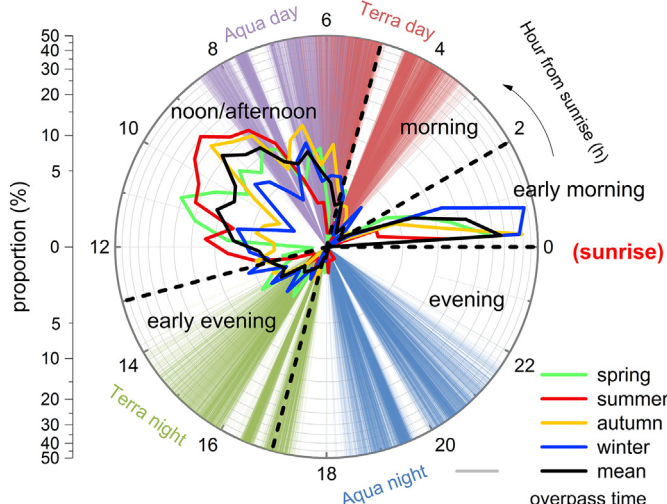


Fig. 3. Frequencies of the estimated t_{\max} within a daily cycle plotted as a polar diagram, with the angular and radial coordinates denoting t_{\max} from sunrise (unit: h) and the corresponding proportion, respectively. The overpass times of the four MODIS daily transits relative to sunrise for all the cities are shown in the colored rays. (For interpretation of the references to color in this figure legend, the reader is referred to the web version of this article.)

seasonal changes and relatively low seasonal mean values (i.e., mostly lower than 3.0 K) demonstrated for the I_{\max} , we further clarify that strong SUHIs (SUHII > 3 K) are often observed (Fig. 4), and both the occurrences and the durations of the strong SUHI exhibit large monthly/seasonal variations.

On average, 10% of the cities across China exhibit a strong SUHI, while if documented using only the four transits, strong SUHIs are only observed in 6% of the cities. In the extreme seasons (summer and winter) strong SUHIs occur more often than in the transitional seasons (spring and autumn). Considerably higher proportions were found in certain climate zones: for example, > 50% of the cities within the Arid Temperate zone exhibit strong SUHIs from November to January. Among all the cities with a strong SUHI in at least one month, the duration was $5.6 (\pm 4.0)$ hours on average (\pm standard deviation). Further, compared with the occurrences of the strong SUHI, its duration exhibits larger monthly/regional variations. Typically, in winter, durations for the northern cities are longer compared to those for the southern cities, with strong SUHI usually exceeding 10 h. Such long durations probably result from the extensive anthropogenic heating flux during the cold months, which maintain high SUHIs throughout the nighttime. In the two transitional seasons, which are warmer, a similar phenomenon is observed, but the north-south contrast is slightly weaker. By contrast, in summer, the longest durations of the strong SUHI appear mainly in southern China; this is presumably related to the enhanced urban-rural contrasts in NDVI that amplify the cooling effect of vegetation for southern cities during this season.

4.1.2. Daily minimum SUHII

The daily minimum SUHIs (I_{\min}) and the associated occurrence times (t_{\min}) over all the cities are shown in Fig. 5. t_{\min} is most likely to occur in the early morning (within 2 h after sunrise) and in the noon/afternoon (i.e., 5 to 13 h after sunrise). More precisely, 50%, 70%, 55%, and 30% of the cities have an early-morning I_{\min} during spring, summer, autumn, and winter, respectively; and the corresponding proportions reach 10–40% per season for the noon/afternoon hours. Further, it also often occurs in the morning with 5% to 30% of the cities recording a t_{\min} at that time. By comparison, during nighttime (i.e., 13 to 24 h after sunrise), t_{\min} is found frequently only in spring and summer while it is almost absent in the autumn and especially winter, which is probably because of the more pronounced nocturnal SUHI in

these two seasons (more explanations are provided in Section 4.2).

We note that the frequency distributions of t_{\min} occasionally overlap with those of t_{\max} (e.g., in the early morning and noon/afternoon) and that both rarely occur around the overpass time of the Aqua-night transits (Fig. 6). In contrast to I_{\max} , the other three MODIS daily transits can all potentially capture I_{\min} in a specific season. Nevertheless, > 45% of the cities exhibit a t_{\min} that matches none of the four transits. In other words, I_{\min} is also likely to be distorted (i.e., overestimated) directly from the four observations, and the occurrences of the SUCI are likely underestimated. Moreover, the seasonal mean I_{\min} values for all cities are negative across the yearly cycle (-0.3 , -0.2 , -0.3 and -0.5 K in spring, summer, autumn and winter, respectively).

The percentages of cities in which an SUCI occurs as well as the monthly mean SUCI durations within an annual cycle are shown in Fig. 7. On average, an SUCI occurs in > 50% of the cities (exceeding 70% in winter), which is much higher than the proportions of cities where an SUCI is observed directly through the MODIS observations (35% on monthly average). Thus, the proportions are also much greater than in previous reports based on the original four transits, which found only 8% (5%) of the cities globally had a daytime (nighttime) SUCI, from an annual perspective (Peng et al., 2012).

From a zonal perspective, SUCIs appear more frequently in the northern bioclimatic zones than in the southern ones, with the most frequent occurrences observed for cities within the Arid Temperate and Plateau Temperate zones. Specifically, all the cities in the Arid Temperate zone exhibit SUCIs during most months, and mean I_{\min} across these cities is lower than -5.0 K for all four seasons. For the Plateau Temperate zone, each month SUCIs arise in over 85% of cities. In comparison, SUCI durations are more similar between cities. The durations of SUCIs generally reach $7.6 (\pm 6.1)$ hours when monthly averaged, and for 60–80% of the cities in which SUCIs emerge, it lasts < 9 h. Nevertheless, SUCIs can occasionally persist for much longer; e.g., in cities in the Arid Temperate and western Mid Temperate zone, and in cities in southwestern China (i.e., the western Southern Subtropical and Mid Subtropical zones) in spring and winter.

4.2. Identified typical DSUHI temporal patterns

Large geographic differences are evident in the daily maximum and minimum SUHIs, especially between southern and northern cities, and the DSUHI variations were, therefore, clarified related to latitude (refer to the Supplementary Information for more details). In particular, it is the latitude-related local bioclimate (including radiation, temperature, precipitation and type of rural background) that partly regulates these DSUHI variations (Zhao et al., 2014). We therefore investigated the DSUHI variations within seven different bioclimatic zones and identified five typical patterns: *standard-spoon*, *weak-spoon*, *quasi-spoon*, *inverse-spoon*, and *straight-line* patterns, (see Figs. 8 and 9). These five patterns are differentiated primarily according to the daytime SUHII dynamics because the nighttime SUHII variations are smaller than those of the daytime dynamics, and the detailed criteria are provided in Table 2. From the zonal perspective, the DSUHI temporal patterns exhibit a general trend that changes from spoon-like patterns (including *standard-spoon*, *weak-spoon* and *quasi-spoon* patterns) in the north to *inverse-spoon* or *straight-line* patterns in the south (see Figs. S2 to S4 given in Supplementary information). Naturally, these patterns represent a continuum, and as in any classification, intermediate patterns may exist. Moreover, the patterns considered here each represent the average diurnal course of all cities within one bioclimatic zone, while the variation between cities is large; thus, certain cities may exhibit patterns that are different from the average pattern.

4.2.1. Standard-spoon pattern

The standard-spoon pattern is defined as the DSUHI temporal pattern with a deep valley during the day and a gradually increasing but relatively stable intensity at night. This pattern is only present in the

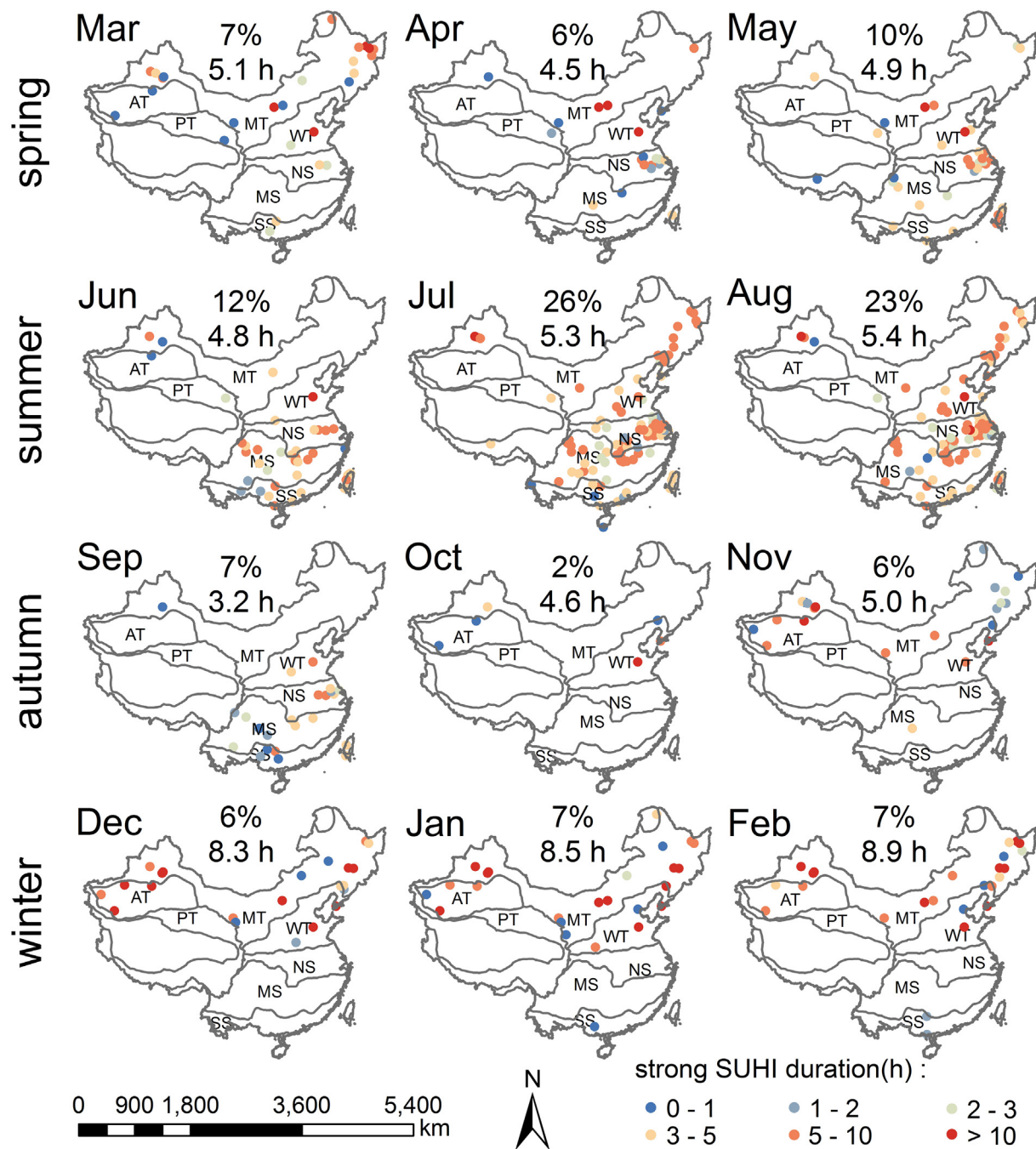


Fig. 4. Monthly mean durations of strong SUHIs ($SUHII > 3.0 K$) within a yearly cycle. The dots represent cities where strong SUHIs are observed in each month, and the dot color indicates the corresponding duration. The percentages as well as the numbers above each subplot represent the proportions of cities with a strong SUHI relative to the total number of the cities in that month and the averaged durations of the strong SUHIs among these cities. (For interpretation of the references to color in this figure legend, the reader is referred to the web version of this article.)

Arid Temperate zone for all four seasons (Fig. S2). It exhibits the greatest rate of change in $SUHII$ (i.e., $\Delta I/\Delta t$) among the five patterns (Fig. 9b): The SUHIs decline rapidly after sunrise, reach minima around noon (i.e., 4 to 8 h after sunrise), increase rapidly before sunset and have a relatively slow rise throughout the night (Fig. 8a).

This pattern typically exhibits a daytime SUCI and an intense nocturnal SUHI all year-round, yet significant seasonal discrepancies exist (Fig. S2). First, the summer has both the most intense SUCI (mean intensity is $-7.5 K$ for all cities in the Arid Temperate zone) as well as the longest SUCI duration (around 12 h, i.e., from 2 to 14 h after sunrise). Conversely, the winter SUCI has the lowest intensity and shortest duration (around $-3.0 K/6 h$). Second, the nighttime SUHII is

comparatively higher during winter, spring and autumn (reaching around $3.0 K$ before sunrise) than in summer (around $2.0 K$).

The rapid decrease in daytime SUHII after sunrise and the formation of a significant daytime SUCI are probably because of the pronounced positive urban-rural contrast in vegetation status as well as the low thermal inertia of the bare land in the Arid Temperate zone. This urban-rural difference in terms of their different land-cover types has also been demonstrated over cities within similar bioclimatic zones, e.g., cities with an arid climate (Lazzarini et al., 2013; Haasemi et al., 2016; Mathew et al., 2018). The seasonal differences between the daytime SUCIs may be attributable to contrasts in urban-rural vegetation due to phenological contrasts. The switch from the SUCI back to the SUHI

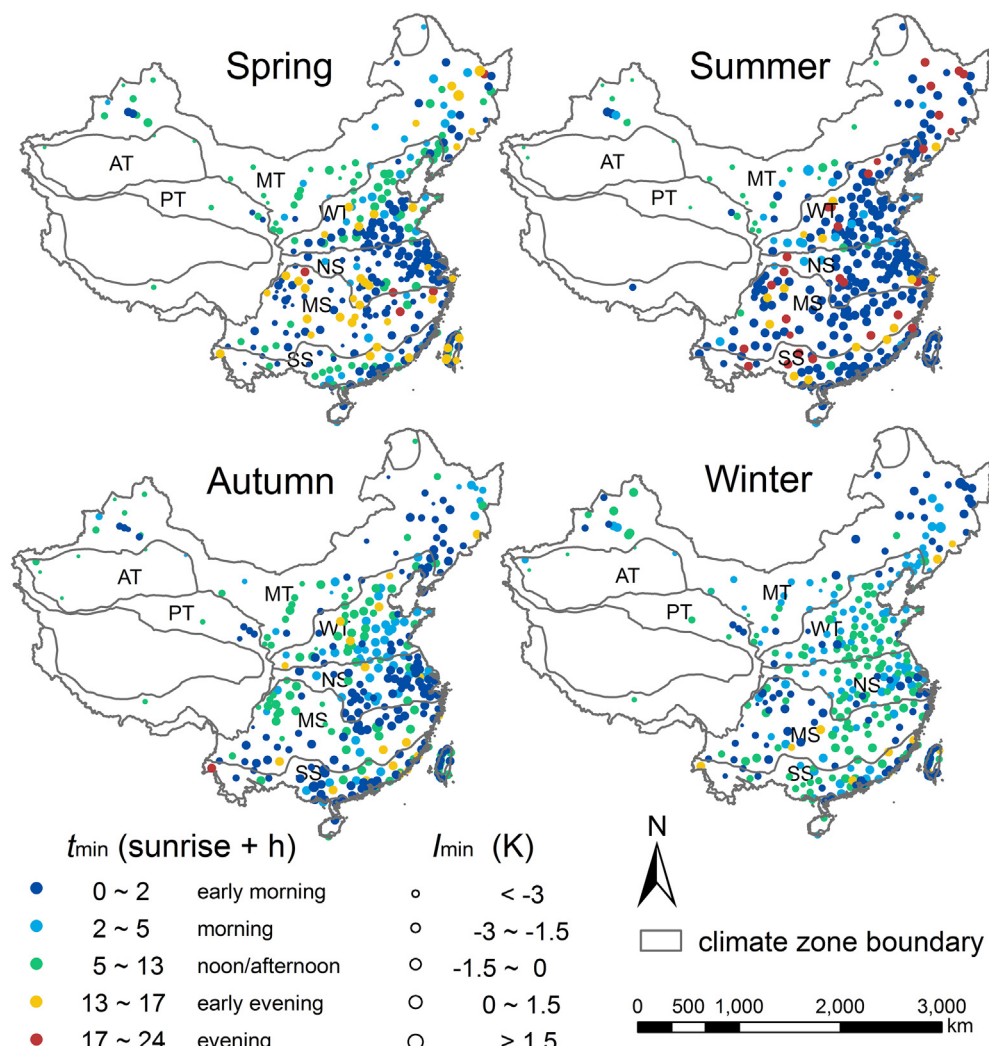


Fig. 5. The minimum SUHII (I_{\min}) and their occurrence time (t_{\min}) for all cities. The dot size represents I_{\min} and the color indicates the period within which t_{\min} occurs. (For interpretation of the references to color in this figure legend, the reader is referred to the web version of this article.)

during the night may be due to the urban canyon effect and anthropogenic heating, since they are the two major controls that preserve more urban heat storage compared to the rural situation. The more significant nocturnal SUHI during winter (near 4.0 K) is likely related to the greater heat emissions from residential areas. Further discussion of the controls of the DUSHI patterns is given in Sections 4.3 and 4.4.2.

4.2.2. Weak-spoon pattern

The weak-spoon pattern is defined as the DSUHI temporal pattern with a general valley during the day and an approximately constant SUHII during the night. This pattern is very common in the three temperate climate zones: it appears in spring, summer, and autumn in the cities in the Plateau Temperate zone, throughout the year in Mid Temperate zone cities, and in spring, autumn and winter in Warm Temperate zone cities (Fig. S3); while it only occurs in the winter in the cities in a single subtropical zone (i.e., the Northern Subtropical zone) (Fig. S4). For this pattern, the SUHII also declines after sunrise, reaches a minimum at around noon, increases in the afternoon, and maintains a sustained maximum during the night (Fig. 8b). The weak-spoon pattern can be distinguished from the standard-spoon in the following aspects. First, the $\Delta I / \Delta t$ of the weak-spoon pattern is much lower in daytime, and even close to zero during the night (Fig. 9b); and second, the mean daytime SUHII for all the cities remain positive, although SUCIs do develop for some individual cities with the weak-spoon pattern (Fig. 8a

vs. b).

Previous studies have also documented the presence of the *weak-spoon* pattern. For example, the summer SUHI for Athens (in the Mediterranean climate zone) exhibited such a pattern, with its t_{\min} around 6 h after sunrise (Sismanidis et al., 2015b). The Beijing metropolis (situated in the Warm Temperate zone), reported by Zhou et al. (2013a) with both geostationary LSTs and MODIS products, also exhibited this pattern on specific days in spring, autumn and winter. Note that in autumn and winter, the associated DSUHI temporal patterns reported in Beijing accord well with the regional mean DSUHI temporal patterns for all the cities within the Warm Temperate zone. Nevertheless, there is still inconsistency in spring, when the *quasi-spoon* rather than the *weak-spoon* pattern occurs in the Warm Temperate zone (further clarification of the *quasi-spoon* pattern is given below). This inconsistency indicates that the DSUHI temporal patterns of a certain city may vary based on the overall regional mean patterns.

4.2.3. Quasi-spoon pattern

The quasi-spoon pattern is defined as the DSUHI temporal pattern with a small valley shortly after sunrise, a small peak in the afternoon, and a relatively steady intensity during the night. This pattern appears in the summer of the cities within the Warm Temperate zone (Fig. S3), and in the autumn within the Northern Subtropical zone (Fig. S4). For this pattern, SUHII have a short-term (around 2 h) decrease after

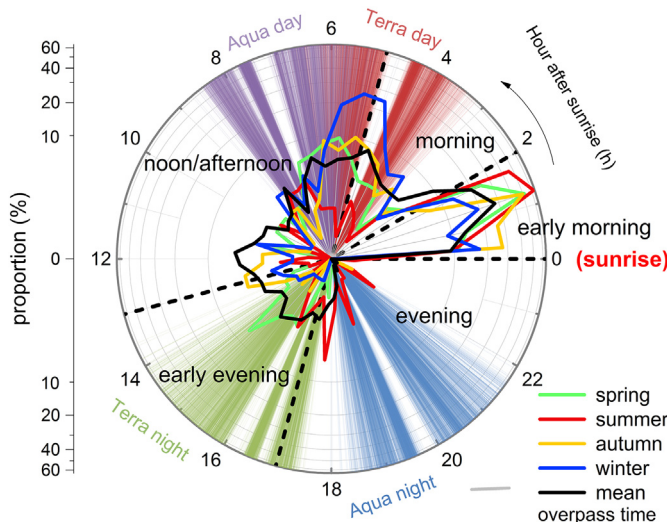


Fig. 6. Frequencies of estimated t_{\min} within a daily cycle plotted as a polar diagram, with the angular and radial coordinates denoting t_{\min} from sunrise (unit: h) and the corresponding proportion, respectively. The overpass time of the four MODIS daily transits relative to sunrise for all the cities is shown by the colored rays. (For interpretation of the references to color in this figure legend, the reader is referred to the web version of this article.)

sunrise, maintain an increasing trend from late morning until near/before sunset, decrease slightly following nightfall, and then preserve a constant and positive intensity during the night (Fig. 8c). The early morning decrease in SUHIs is probably due to the faster heating of rural open land responding to the incipient solar insolation when compared with that over urban areas, which can be delayed by the shading effect of urban buildings when solar altitudes are low (Allen et al., 2017; Oke et al., 2017). Subsequently, the urban shading effect weakens as the solar altitudes gradually increase, so that the SUHIs increase until the more rapid urban cooling weakens them again. Note that for this pattern t_{\max} is often around sunset while t_{\min} may be either in the early morning or in the early evening; and the occurrence of SUCIs is rare.

The *quasi-spoon* pattern was also illustrated for summer in Paris (Zakšek and Oštir, 2012) and Istanbul (Sismanidis et al., 2015b). Nevertheless, for these cities, it generally took longer (around 4 h) for the SUHIs to rebound following the small valley in the morning; and this possibly indicates a larger shading effect of the tall buildings (i.e., the urban geometry may have a more dominant effect over the vegetation abundance for shaping the DSUHI temporal pattern in the morning of these cities).

4.2.4. Inverse-spoon pattern

The inverse-spoon pattern is defined as the DSUHI temporal pattern with a general peak during the day and a roughly constant intensity at night. This diurnal pattern only appears for the cities in the subtropical zones, including spring and summer of the Northern Subtropical zone, spring, summer and autumn of both the Mid Subtropical and Southern Subtropical zone (Fig. S4). This pattern differs from all others in that it has a constantly positive SUHII change rate for the first half of the daytime (Fig. 9b). The SUHII increases after sunrise, reaches a peak in the early afternoon (8 to 10 h after sunrise), weakens in the afternoon until the first half of the night, and rarely changes during the second half of the night (Fig. 8d). The completely reverse regime of this pattern, compared to the previous spoon-like patterns, probably results from the higher vegetation abundance in the rural areas.

For this pattern, we further observed that the SUHII growth rate is occasionally small and may become negative within a short period (around 2 h) after sunrise. Such an early-morning decline was also

reported from ground-based measurements in Basel (Allen et al., 2017) and Vancouver (Allen, 2017), where the summer DSUHIs exhibited a similar *inverse-spoon* pattern. Like the short-term decrease for the *quasi-spoon* pattern after sunrise, extensive shading induced by buildings is also assumed to be the dominant factor causing the early-morning decline. The *inverse-spoon* pattern was also observed from satellite-based measurements during the summer season in Beijing (Zhou J. et al., 2013) and Rome (Sismanidis et al., 2015b).

4.2.5. Straight-line pattern

The straight-line pattern, as its name implies, is defined as the DSUHI temporal pattern with an approximately constant intensity throughout the day. This pattern was observed mostly for cities within the subtropical zones: it appears in the winter for cities within the Mid Subtropical zone as well as those within the Southern Subtropical zone (Fig. S4); while it is only shown for those cities within the Plateau Temperate zone in winter (Fig. S3). This pattern is characterized by very small variations during the diurnal cycle with the mean SUHII always being around 0.5 K (Fig. 8e). To the best of our knowledge, no instances of this pattern have been observed in previous DSUHI studies.

4.3. Analysis of the controls of DSUHI temporal patterns

The DSUHI temporal patterns are calculated as the difference between the urban and rural LSTs within diurnal cycles, as identified in Section 4.2, and these patterns are regulated in theory by the four controlling parameters of the GOT09_A model (i.e., T_0 , T_a , t_m and t_s) over both urban and rural surfaces (Hong et al., 2018). The daily mean SUHIs are speculated to be partly determined by the urban-rural contrast in the residual temperature T_0 (i.e., ΔT_0 , wherein Δ represents the urban-rural difference), but the DSUHI temporal patterns are less impacted by ΔT_0 , which is the constant term in the four-parameter DTC model and therefore controls only the magnitude rather than the shape of the DSUHI. By comparison, the urban-rural difference in the daily temperature amplitude (ΔT_a) is anticipated to have a large impact on the DSUHI temporal patterns because ΔT_a determines the diurnal variations in the magnitudes of the SUHIs (e.g., whether a spoon-/inverse-spoon- or straight-line-like pattern is exhibited). Similarly, DSUHI temporal patterns are expected to be influenced by the urban-rural difference in the daily peak LST time (Δt_m) and the time when the LST begins to attenuate (Δt_s), which, in combination with ΔT_a , collectively regulates the t_{\max} and t_{\min} of the diurnal SUHII dynamics shown in Figs. 2 and 5.

The analysis of the controls of DSUHI temporal patterns is therefore related to those of the controls of ΔT_a , Δt_m , and Δt_s . Studies by Jin and Dickinson (1999) and Duan et al. (2014) have illustrated that these three parameters are closely related to the urban-rural contrast in vegetation status represented by NDVI. The urban-rural contrast in NDVI (ΔNDVI) is also significantly related to the daytime SUHII (Li et al., 2011; Wang et al., 2015; Weng et al., 2011; Yuan and Bauer, 2007). It is therefore anticipated that it would govern DSUHI temporal patterns, especially in the vegetation growing season. To test this hypothesis, summer Beijing was chosen as an example to derive the possible variations of the DSUHI temporal patterns governed by different ΔNDVI (please refer to Section 3.2.4 for the methodology). The corresponding results are displayed in Fig. 10.

The interpretation of the following analysis is presented based on the sign of ΔNDVI .

(1) Urban NDVI is lower than rural NDVI ($\Delta \text{NDVI} < 0$)

In this case, the DSUHI mostly exhibits an *inverse-spoon* pattern (see Lines a_1-a_4 , Lines b_1-b_3 , Lines c_1-c_2 and Line d_1 in Fig. 10). For these lines, the daytime SUHIs generally increase rapidly after a short-term decrease after sunrise. The increase is a result of the faster urban heating of impervious surfaces (e.g., buildings and streets) compared

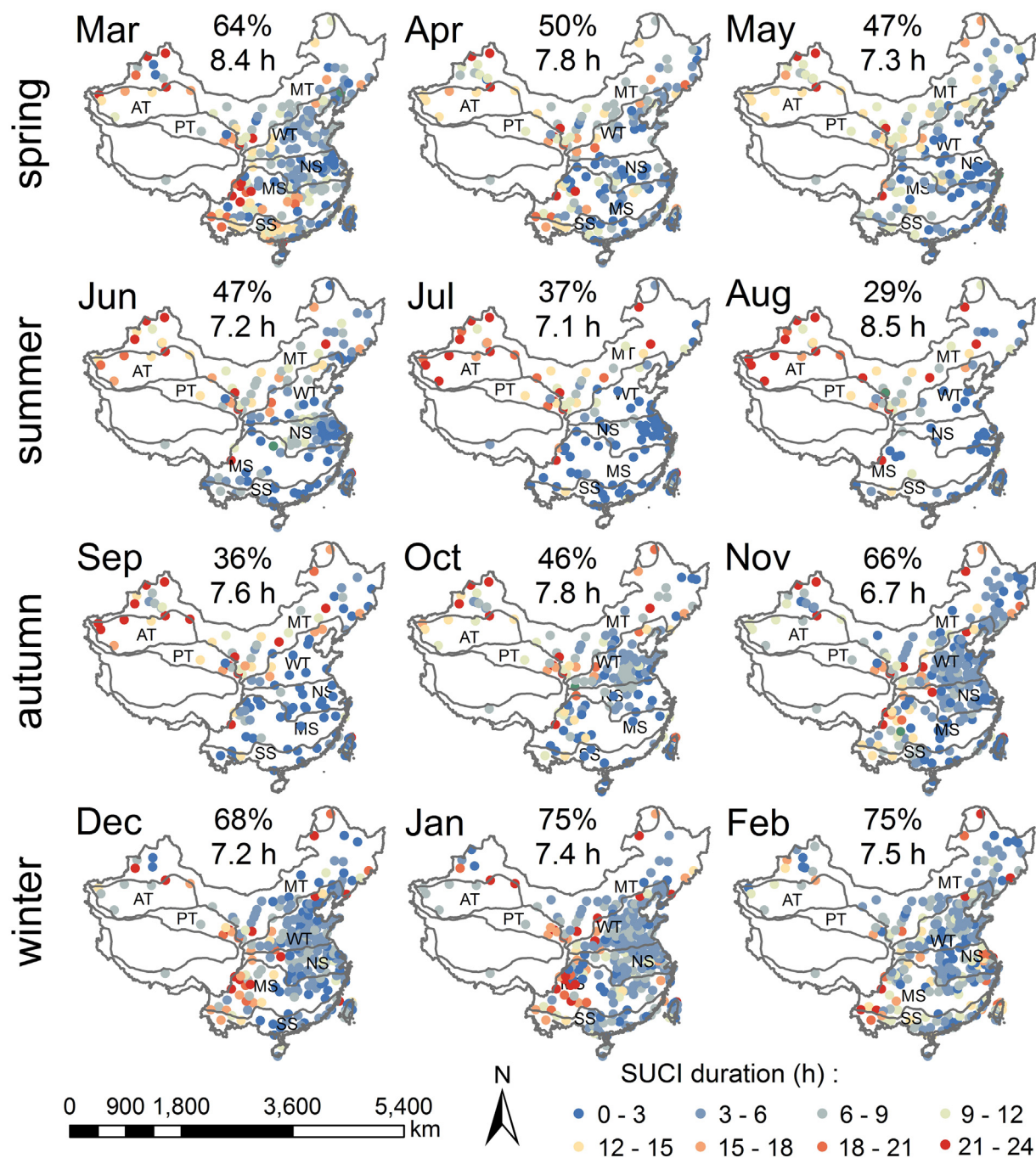


Fig. 7. Monthly mean durations of SUCIs ($SUHII < 0.0 K$) within a yearly cycle. The dots represent the cities where SUCIs are displayed for each month, and the dot color indicates the associated duration. The percentages, as well as the numbers above each subplot, represent the proportions of cities displaying an SUCI relative to the total number of the cities in that month and the averaged durations of the SUCIs among these cities. (For interpretation of the references to color in this figure legend, the reader is referred to the web version of this article.)

with rural heating, which is suppressed by the cooling effect of the greater prevalence of vegetation (see also Figs. 8d and 9a). In the afternoon, the rapid cooling of urban areas forces the SUHII to decrease, while later, the canyon effect as well as anthropogenic heat inputs slow urban cooling and help maintain a moderate SUHII throughout the night.

(2) Urban NDVI is approximately equal to rural NDVI ($\Delta NDVI \approx 0$)

In this scenario, the DSUHI exhibits a *straight-line* pattern (see Lines a_5 , b_4 , c_3 , and d_2 in Fig. 10). The *straight-line* pattern suggests that the

overall urban and rural heating/cooling rates become generally similar when the urban and rural NDVI values are roughly equal and high. This result is expected because, in this case, evaporative cooling due to vegetation is generally equivalent over urban and rural areas. This result also indicates that vegetation-induced cooling surpasses the impacts from the other factors (e.g., urban geometry and anthropogenic heat input) when urban and rural vegetation coverages are at the same level.

(3) Urban NDVI is greater than rural NDVI ($\Delta NDVI > 0$)

For this situation, which often corresponds to cities in desert or arid

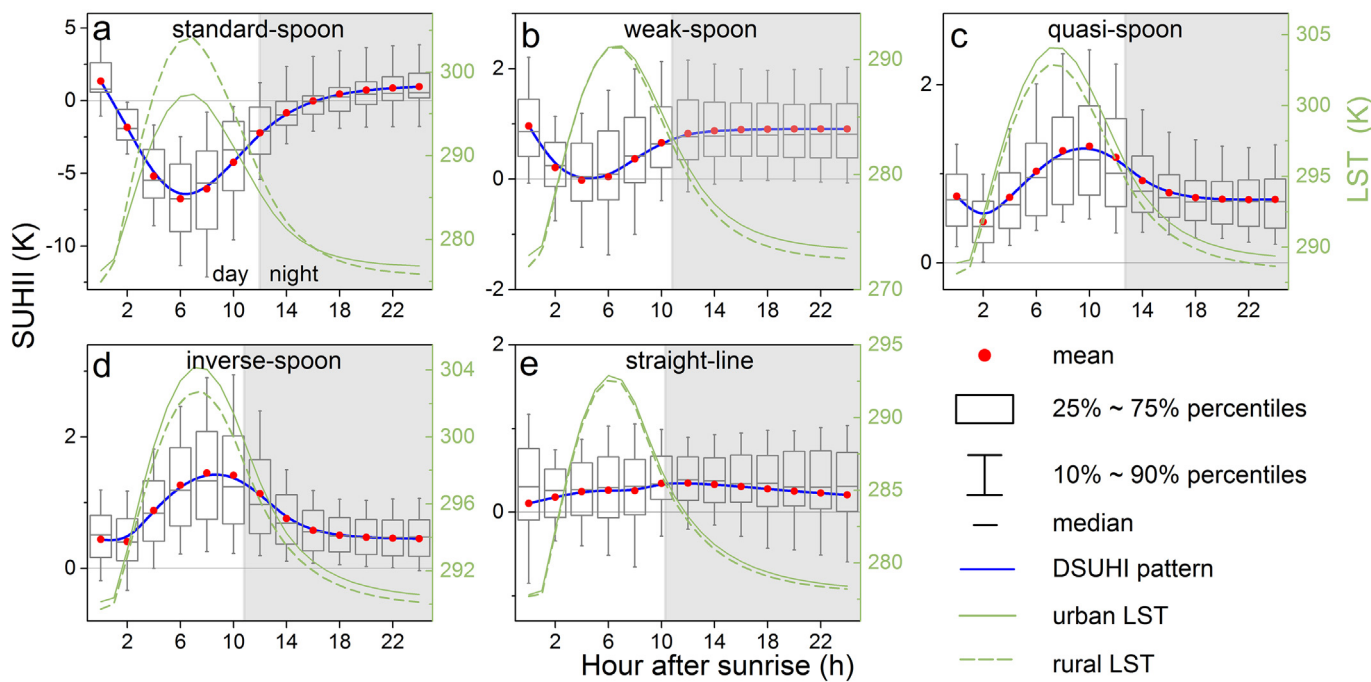


Fig. 8. Five typical DSUHI temporal patterns and their associated diurnal urban/rural LST cycles in China. Note that for each pattern, the boxplot includes the seasonal DSUHI variations of every city within the bioclimatic zones that was classified as possessing this pattern. The DSUHI temporal pattern was calculated as the mean DSUHI values for all these cities, and the urban/rural LSTs are the associated mean urban/rural LSTs among these cities. The grey shading represents nighttime.

zones, the DSUHI exhibits a *standard-* or *weak-spoon* pattern (see Lines b_5 , c_4-c_5 and d_3-d_5 in Fig. 10). For these lines, the daytime SUHII after sunrise decreases and can become negative (occurrence of an SUCI) due to the rapid heating of rural bare soils under significant solar insolation when compared to more vegetated urban areas (Fig. 9a). The SUCI weakens, and a SUHI returns at night, which is once again probably attributable to the urban canyon effect.

By examining the DSUHI dynamics for a single city, the above analysis clarifies that the DSUHI temporal patterns are mainly regulated by the urban-rural contrast in vegetation status. Such controls were further confirmed by the close relationship between Δ NDVI and the durations of strong SUHIs and SUCIs in certain seasons (see Fig. S5). Although the controls from NDVI on the DSUHI temporal patterns have been explained reasonably well, we nevertheless note that no significant relationships were found between the two DSUHI descriptors, i.e., t_{\max} and t_{\min} , and Δ NDVI. This result may be partly attributable to

the high sensitivities of these two DSUHI descriptors to the quality of LST inputs as well as to the accuracy of the four-parameter DTC models (further explanation is given in Section 4.4.1). Further, the DSUHIs are also controlled by factors other than NDVI, such as the urban geometry, background climate, properties of the rural background, urban structures, and anthropogenic heat (additional discussion of the controls of the DSUHIs is provided in Section 4.4.2) (Clinton and Gong, 2013; Imhoff et al., 2010; Li et al., 2011; Liu et al., 2017; Oke, 1982; Peng et al., 2012; Schwarz and Manceur, 2015; Zhou et al., 2017).

4.4. Discussion

With the assistance of the polar-orbiting satellite products and the latest four-parameter DTC model that has the highest accuracy, this study has identified five typical patterns for the DSUHI from a clear-sky climatological perspective over more than three hundred cities. To our

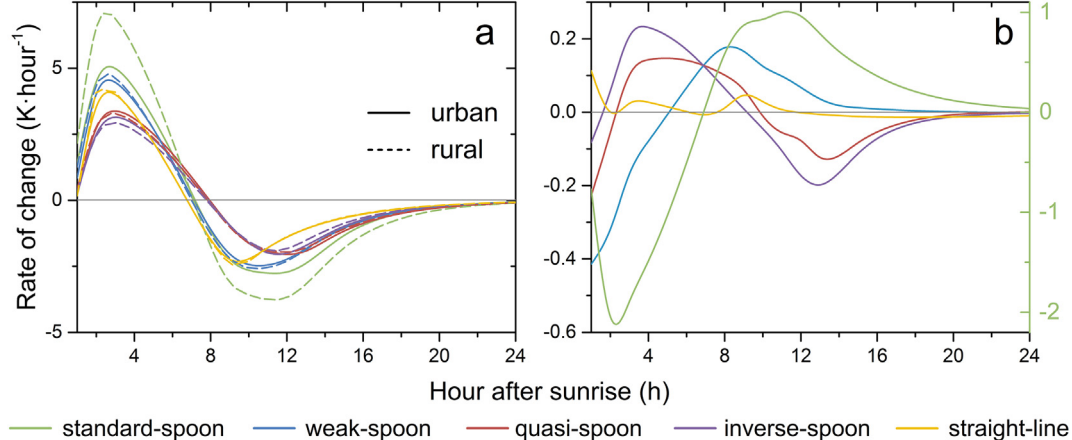


Fig. 9. Rates of change in (a) urban and rural LSTs and (b) SUHIs plotted for the five identified DSUHI temporal patterns within a daily cycle. Note that for subplot b, the left y-axis refers to the changing rate of the *weak-spoon*, *quasi-spoon*, *inverse-spoon*, and *straight-line* patterns, while the right y-axis refers to that of the *standard-spoon* pattern.

Table 2

Criteria for differentiating the five typical patterns.

Pattern	Morning	Noon	Afternoon	Evening
Standard-spoon	$\Delta I/\Delta t < 0$ and can exceed -1 K/h ; SUCI appears	$\Delta I/\Delta t$ transits from < 0 to > 0 ; I_{\min} appears; SUCI lasts	$\Delta I/\Delta t > 0$	$\Delta I/\Delta t > 0$ but is close to zero
Weak-spoon	$\Delta I/\Delta t < 0$ but never exceed -1 K/h	$\Delta I/\Delta t$ transits from < 0 to > 0 ; I_{\min} appears	$\Delta I/\Delta t > 0$	$\Delta I/\Delta t$ is close to zero
Quasi-spoon	$\Delta I/\Delta t$ transits from < 0 to > 0	$\Delta I/\Delta t > 0$	$\Delta I/\Delta t$ transits from > 0 to < 0	$\Delta I/\Delta t$ transits from < 0 to close-to-zero
Inverse-spoon	$\Delta I/\Delta t > 0$ (occasionally < 0 shortly after sunrise)	$\Delta I/\Delta t > 0$	$\Delta I/\Delta t$ transits from > 0 to < 0 ; I_{\max} appears	$\Delta I/\Delta t$ transits from < 0 to close-to-zero
Straight-line	$-0.3 < \Delta I/\Delta t < 0.3 \text{ K/h}$, and no specific regime is present throughout the diurnal cycle			

knowledge, this is the first study to incorporate cities with a wide variety of urban morphology, rural background, and biophysical conditions. By a comprehensive examination and comparison of the DSUHI temporal patterns, our results contribute to the understanding of the less well-studied SUHI temporal dynamics (i.e., the true diurnal dynamics). The derived DSUHI temporal patterns also allow for the identification of the daily maximum and minimum SUHIs and the associated occurrence times even if there are no overpassing satellites. These variations, when combined with in-situ meteorological observations (e.g., air temperature, wind, humidity, and radiation), may provide insight into the diurnal variation of large-scale physiological equivalent temperatures (PETs), which directly relate to the thermal comfort of humans. Moreover, the durations of the strong SUHIs and SUCIs can be estimated so that the effect of urbanization on energy consumption used in urban heating/cooling can be better characterized (Akbari and Konopacki, 2005), and the times when UHI mitigation are most needed can be identified.

Our results reveal that the DSUHI demonstrates a much greater variety of patterns when compared with the DCUHI, as also evidenced by the detailed comparison of the DSUHI and DCUHI patterns over the nine megacities (see Fig. S6). GST measurements can as well be suitable

for the identification of DSUHI temporal patterns, but this type of measurement suffers from its low density and lower degree of representativeness of true urban surfaces (refer to Supplementary Information); thus, the use of such GSTs will probably distort DSUHI interpretations. To resolve the issue of representativeness, Allen et al. (2017) suggested the use of pyrgeometers since their hemispherical FOV captures a much larger sample of surfaces than a typical infra-red temperature radiometer. Nevertheless, the cost of the installation of many pyrgeometers over extensive urban surfaces can be high, and the process of correction for atmospheric effect may also induce uncertainties. With LSTs from polar-orbiting satellites, the *DTC modeling* strategy provides a simple yet effective way to conduct DSUHI examinations. Our evaluations also show that the DSUHI temporal patterns over Beijing obtained using the *DTC modeling* and *spatial downscaling* strategies (Zhou J. et al., 2013) are similar. Though progress in identifying and understanding the DSUHI temporal patterns has been made, limitations remain, and clarification of the uncertainties and/or prospects of this investigation are given below.

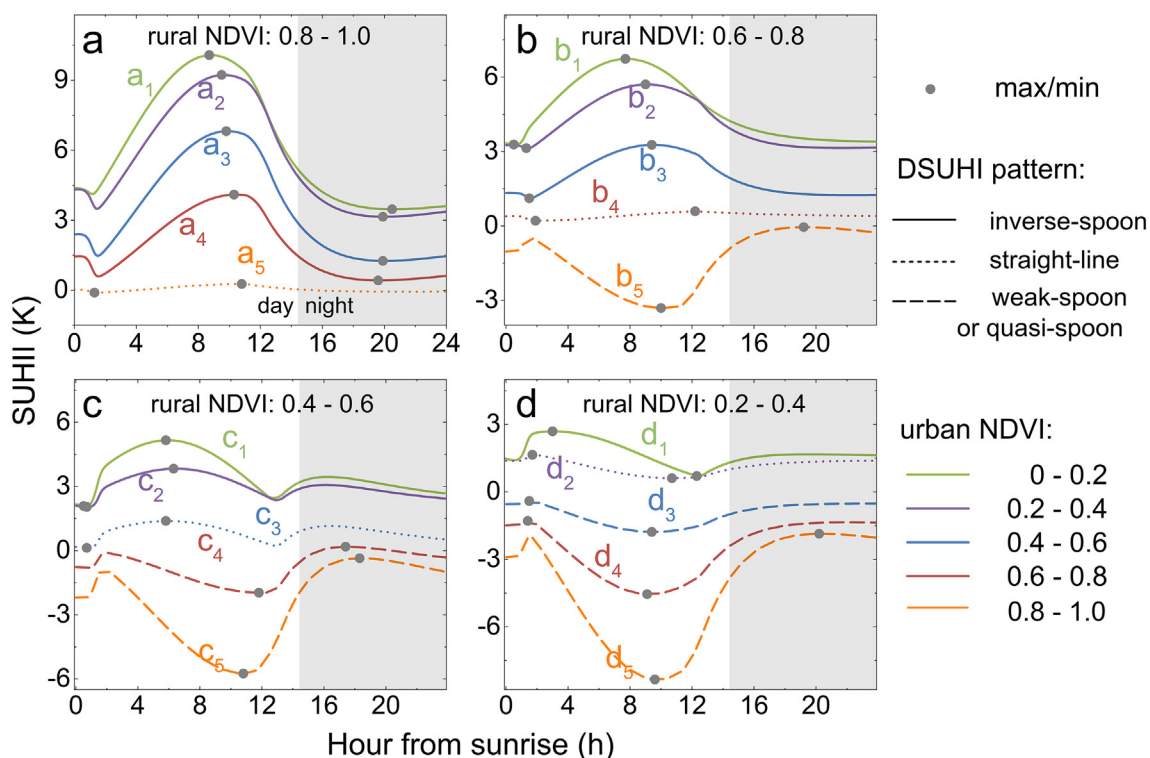


Fig. 10. Variations in DSUHI temporal patterns (lines a₁-a₅, b₁-b₅, c₁-c₅ and d₁-d₅) for summer in Beijing under different combinations of urban and rural pixels classified by NDVI values. Each DSUHI temporal pattern is calculated as the difference between the mean LST of the urban and rural pixels with the corresponding category of NDVI values.

4.4.1. Uncertainties induced by satellite-derived LSTs and the four-parameter DTC model

Although MODIS products such as LSTs have been widely considered to have a relatively high accuracy (Wan, 2008), the accuracies of these products, especially those with slanted observation angles, may become lower over heterogeneous urban surfaces due to significant urban thermal anisotropy (Hu et al., 2016; Voogt, 2008). Studies have indicated that the LST biases induced by this thermal anisotropy may reach 5.0 K and may be even higher over city cores with tall buildings (Lagouarde et al., 2010; Zhan et al., 2012). This uncertainty in the MODIS LSTs will therefore likely distort the interpretations of DSUHI temporal patterns. However, in this study, a temporal aggregation of the MODIS LSTs at the monthly or seasonal scales was conducted prior to the DTC modeling, and we also implemented a composition of the LSTs under different viewing angles, which will greatly reduce the LST biases due to thermal anisotropy. Consequently, the effects of such distortions on our interpretations are likely minimal (Hu et al., 2016). Another control that will likely change the DSUHI temporal pattern is the antecedent weather conditions, especially any that yield precipitation. Studies have illustrated that precipitation is able to greatly weaken SUHI effects during the precipitation process while the SUHI effect is strengthened afterwards (He, 2018). It is therefore anticipated that preceding precipitation can likely bias the DSUHI descriptors (e.g., the I_{\max} , I_{\min} , strong SUHI/SUCI duration). Nevertheless, we consider that the impacts due to the preceding precipitation may be considerably diminished when a large number of LST images are aggregated, and despite the possible alterations to the DSUHI descriptors, the identified typical DSUHI temporal patterns are likely robust.

Comprehensive comparisons have exemplified that the four-parameter DTC model used in this study (i.e., the GOT09_A) has the best performance and stability among all available models (Hong et al., 2018). In addition, with the temporally composited LSTs, the parameter reduction schemes used by GOT09_A are more reasonable and the associated model accuracy is further guaranteed, as explained in Section 3.2.1. Nevertheless, four-parameter DTC models oversimplify the diurnal LST dynamics, and model uncertainties exist in GOT09_A, especially for the period shortly after sunrise, despite its considerably better ability to depict LST dynamics compared to other four-parameter DTC models (Hong et al., 2018). Such an over-simplification will likely yield biases in the resultant DSUHI and therefore DSUHI descriptors (e.g., t_{\max} and t_{\min}), which are sensitive to DSUHI fluctuations. Although uncertainties may appear in some DSUHI descriptors, the typical DSUHI temporal patterns that were identified will probably remain credible. This credibility is also justified by Fig. A1 in the Supplementary Information, which illustrates that the geostationary-derived and MODIS LST-derived DSUHI temporal patterns are mostly similar in several megacities, despite the considerable discrepancies in the accuracies and spatial resolutions between these two different data sources.

In addition, the *DTC modeling* strategy provides only smoothed DSUHI temporal patterns from a climatological perspective. The real DSUHI temporal pattern over a specific city and on a specific day may vary depending on the property and synoptic conditions of the city (further explanations are provided in Sections 4.4.2 and 4.4.3). The *spatial downscaling* strategy based on high-frequency geostationary LSTs, if its relative difficulty/complexity is ignored, can potentially help derive the DSUHI temporal patterns with higher accuracy for specific cities (Bechtel et al., 2012; Keramitsoglou et al., 2013; Sismanidis et al., 2015a, b; Zákašek and Ošťíř, 2012; Zhou J. et al., 2013). Moreover, with the recently launched Himawari-8 satellite and the new-generation geostationary satellites in preparation, LST observations with a spatial resolution of 2 km can be produced every 15 min. These high-frequency LSTs can be directly used for DSUHI investigations over megacities even without spatial downscaling and DTC modeling procedures. However, care is needed when interpreting DSUHI temporal patterns derived from geostationary observations because these satellites always observe

cities from fixed directions, and the induced urban thermal anisotropy may distort DSUHI interpretations (Hu et al., 2016). Geostationary observations may be inappropriate for the study of SUHIs at high latitudes and therefore for the investigation of DSUHI temporal patterns of cities on a continental/global scale.

4.4.2. Clarifications on other controls of DSUHI temporal patterns

The typical DSUHI temporal patterns have been elucidated under the dominant control of the urban-rural contrast in NDVI, where the spoon-like, straight-line, and inverse-spoon patterns were demonstrated to be governed by a positive, near-zero, and negative Δ NDVI, respectively. Nevertheless, we clarify that DSUHI variations are actually influenced by a combination of impacts from various controls in addition to vegetation cover. Urban geometry, for example, is the primary control that accounts for the early-morning DSUHI decline through the shading effect of the urban buildings that reduces ground-level solar insolation and surface temperatures in the early morning in more densely built neighbourhoods, especially during winters for cities at higher latitudes (Allen et al., 2017); it can also help preserve nocturnal heat storage and, as a result, strengthen the nighttime SUHI. Similarly, controls such as urban structures, building materials, and distances to water bodies can also influence SUHI effects (Schwarz and Manceur, 2015) and, as a result, lead to variations in the DSUHIs of certain cities in reference to the typical patterns in their corresponding bioclimatic zones. In addition, DSUHI temporal patterns remain sensitive to the elevation/slope of some cities, although the topography impacts have been partly suppressed by removing the pixels with extreme high/low elevations (refer to Section 3.2.3).

Another factor that can exert impacts on DSUHI variations is the rural background in terms of its land cover type and extent, which determine the diurnal temperature dynamics of rural lands. The rural extent is assumed to be capable of affecting, to some extent, the DSUHI descriptors due to their close relationship with the SUHII, as clarified by previous studies (Clinton and Gong, 2013). For example, the I_{\max} may be enlarged over large rural extents, and the durations of both strong SUHI and SUCI effects may also be enlarged due to an intensified diurnal SUHI variation. However, we consider that despite the possible change in the DSUHI descriptors at different rural extents, the typical patterns identified in this study will rarely change in most cases because the rural thermal properties usually remain similar as rural extents increase. The rural land cover type, by comparison, is speculated to affect not only the simultaneously estimated SUHII (Imhoff et al., 2010) but also the DSUHI temporal patterns. For instance, the DSUHI with forests as the only rural land cover type is anticipated to demonstrate a very different pattern from those with other land cover types as the main rural lands (i.e., the patterns identified in this study). As indicated in Section 3.2.3, forests in China strongly correspond to undulating mountains, and their LST dynamics are therefore impacted more by altitude and evaporative cooling compared to regular rural lands. With forests as the only rural background, the considerably lower forest surface temperatures resulting from the high altitude and intensive evaporation can greatly increase daytime SUHII, therefore likely transforming the ‘straight-line’ DSUHI temporal pattern to ‘inverse-spoon’ patterns (Fang et al., 2017).

4.4.3. Clarification of clear-sky climatology vs. all-weather DSUHI temporal patterns

The DUSHI patterns identified in this study only represent the scenario under clear-sky conditions. Previous research has documented that the SUHII, particularly during the daytime, would decrease under cloudy conditions when compared with that observed under clear skies (Allen et al., 2017). By considering both clear-sky and overcast conditions, DSUHI temporal patterns are expected to change, and they may become less typified than the five patterns shown in Section 4.2. For example, the characteristic spoon-like DSUHI temporal pattern shown for cities within the Arid Temperate zones will probably remain, but the

daytime SUCI magnitude will probably decrease under all-weather conditions. To acquire accurate all-weather DSUHI temporal patterns, one may try to generate the LSTs under clouds with available satellite LST products; e.g., using the algorithm proposed by Jin (2000). Moreover, though in-situ high-frequency GST measurements are unsuitable for the study of DSUHI temporal patterns under clear-sky conditions, due to their limited sampling areas (refer to Supplementary Information), these measurements are likely to be more representative of the less heterogeneous thermal status under overcast conditions because of the absence of direct solar radiation. Therefore, another possibility for deriving all-weather DSUHI temporal patterns is the incorporation of in-situ GSTs.

The DSUHI temporal patterns identified in this study were primarily provided from the climatological perspective, i.e., they were presented on a monthly or seasonal scale using temporally aggregated LST data. The daily DSUHI temporal pattern will vary according to synoptic conditions, such as precipitation, cloud coverage and wind speed. For example, the SUHI effect may be completely eradicated on rainy and/or windy days (Zhou et al., 2011), i.e., a *straight-line* pattern is shown. On days after precipitation events, the daytime SUHII can be intensified because of the larger water retention capacity of rural lands, which significantly weakens the heating rate in response to insolation, while the nighttime SUHII may decline because of the large thermal inertia of rural lands suppressing the cooling process (He, 2018). The DSUHI may even exhibit a completely different pattern under specific synoptic situations, such as heat waves. Further investigations are therefore necessary to determine how the DSUHI temporal patterns fluctuate in response to synoptic conditions, as have been presented for CUHI dynamics (Runnalls and Oke, 2000). Based on such investigations, the DSUHI temporal pattern can potentially be predicted using forecasted synoptic conditions (Huang et al., 2016).

5. Conclusions

The diurnal pattern of the SUHI is an important component of urban thermal dynamics on multiple time scales, but the recognition and understanding of the climatology, variety, and taxonomy of DSUHI temporal patterns for various cities over extensive regions have not been studied comprehensively. This study has investigated DSUHIs for 354 megacities with very different bioclimates across China using MODIS LST data as well as a four-parameter DTC model. Our approach provided the spatiotemporal distributions of DSUHI descriptors and identified typical DSUHI temporal patterns. Our results suggest that the diurnal SUHI climatology exhibits a greater variety of patterns than those of the CUHI. More detailed conclusions are summarized as follows:

The daily maximum and minimum SUHI intensities (i.e., I_{\max} and I_{\min}) can both occur at most periods within a daily cycle and they share a relatively higher probability of occurring in the early morning and

noon/afternoon. In addition, the two extreme intensities cannot be captured for more than one-half of the cities by the four MODIS transits due to the mismatch between their occurrence times and the MODIS transit times. Both strong SUHIs ($SUHII > 3 K$) and SUCIs ($SUHII < 0 K$) can be prevalent in China, with the former phenomenon observed for 10% of the cities and the latter observed over 50% of the cities, while by the four transits they are only captured for 6% and 35% of the cities, respectively. Further assessments show that the monthly mean (\pm standard deviation) durations for the strong SUHI and SUCI are $5.6 (\pm 4.0)$ and $7.6 (\pm 6.1)$ hours, respectively; and their occurrences and durations both exhibit large regional and monthly variations.

These DSUHI descriptors are extracted from the associated DSUHI temporal patterns, and in turn they can be used to characterize and then categorize DSUHI temporal patterns. Five typical DSUHI temporal patterns were identified: *standard-spoon*, *weak-spoon*, *quasi-spoon*, *inverse-spoon*, and *straight-line* patterns. These patterns exhibit a clear north-south contrast, with a general transition from spoon-like patterns (*standard-spoon*, *weak-spoon*, and *quasi-spoon* pattern) in the northern temperate bioclimatic zones to the *inverse-spoon* or *straight-line* patterns shown in the southern subtropical zones. Moreover, the category of DSUHI temporal patterns was revealed to be closely related to the urban-rural difference in vegetation status (ANDVI) and the urban canyon effect.

We acknowledge that these DSUHI temporal patterns are limited only to clear sky conditions and are only of climatological significance. By systematically investigating the variety and taxonomy of DSUHI climatology over a large spatiotemporal scales, we nevertheless consider that this study provides insights into the true diurnal dynamics of the SUHI and, as a result, facilitates a more comprehensive interpretation and understanding of SUHI dynamics on multiple time scales.

Acknowledgments

We thank all the institutions that freely provided the data. The MODIS data we used were downloaded at NASA's Earth Observing System and Data and Information System (EOSDIS) (<https://earthdata.nasa.gov/>). The hourly SATs and GSTs in the nine megacities were provided by China Meteorological Data Service Center.

This work is jointly supported by the National Key R&D Program of China under Grant number 2017YFA0603604, National Natural Science Foundation of China under Grant 41671420, National Key R&D Program of China under Grant number 2016YFA0600201, and the Fundamental Research Funds for the Central Universities under Grant number 090414380017. Dr. Benjamin Bechtel was supported by the Cluster of Excellence 'CliSAP' (EXC177), University of Hamburg, funded through the German Science Foundation (DFG). We are also grateful for the financial support provided by the DengFeng Program-B of Nanjing University.

Appendix A

To test the credibility of the identified DSUHI temporal patterns, we further compared the DSUHI temporal patterns using the FY-2F and MODIS LSTs in three megacities (refer to Fig. 1 for their locations). The results of this comparison are provided in Fig. A1.

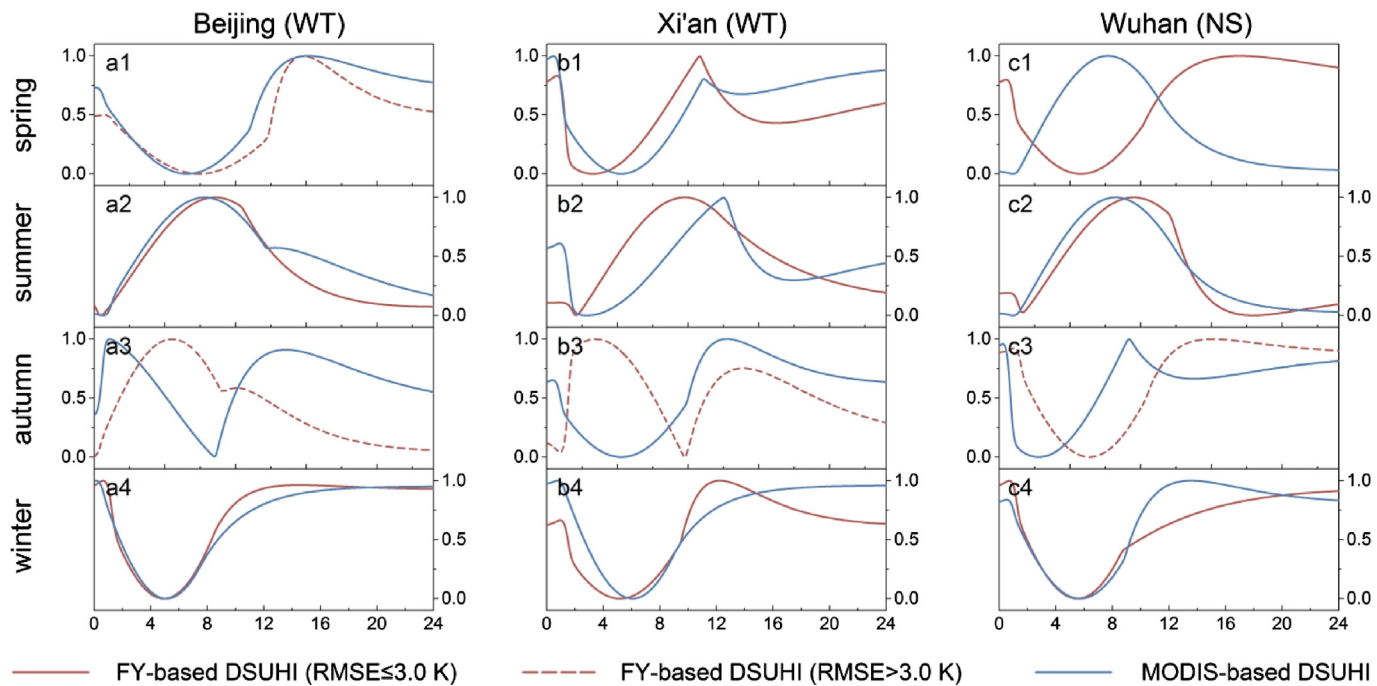


Fig. A1. Comparison of the seasonal mean DSUHI temporal patterns derived using the FY-2F and MODIS LSTs in 2016 over three megacities including Beijing (a1 to a4), Xi'an (b1 to b4), and Wuhan (c1 to c4). The FY-based DSUHI temporal patterns plotted as dashed lines denote the cases when the DTC modeling RMSE is unreasonably high (i.e., larger than 3.0 K).

These results indicate that the MODIS-based DSUHI temporal patterns strongly correspond with those from FY-2F in most cases once the DTC modeling RMSE of the FY data is smaller than 3.0 K, especially during the extreme seasons (i.e., the summer and winter). One exception is for the spring in Wuhan, when the DSUHI temporal patterns identified from these two different data sources display opposite patterns. The appearance of such discrepancies may be due to the following two reasons: First, although the geostationary-based DTC modeling RMSE for this scenario is < 3.0 K, a small portion of abnormal LST observations was still found, which would probably distort the modeled SUHIs. Second, considerable large lakes/water bodies exist within and around Wuhan, which may exaggerate the co-registration issue as well as the difference in spatial resolution between these two different LSTs, therefore leading to discrepancies in the DSUHI temporal patterns.

Appendix B. Supplementary data

Supplementary data to this article can be found online at <https://doi.org/10.1016/j.rse.2018.08.021>.

References

- Akbari, H., Konopacki, S., 2005. Calculating energy-saving potentials of heat-island reduction strategies. *Energ Policy* 33 (6), 721–756. <https://doi.org/10.1016/j.enpol.2003.10.001>.
- Allen, M.A., 2017. A Method for Hemispherical Ground Based Remote Sensing of Urban Surface Temperatures. Western University, Canada, pp. 4594. <http://ir.lib.uwo.ca/etd/4594> (MSc. Thesis, Electronic Thesis and Dissertation Repository).
- Allen, M.A., Voogt, J.A., Christen, A., 2017. Time-continuous hemispherical urban surface temperatures. *Remote Sens.* 10 (1), 3. <https://doi.org/10.3390/rs10010003>.
- Anniballe, R., Bonafoni, S., Pichierri, M., 2014. Spatial and temporal trends of the surface and air heat island over Milan using MODIS data. *Remote Sens. Environ.* 150 (150), 163–171. <https://doi.org/10.1016/j.rse.2014.05.005>.
- Bechtel, B., 2015. A new global climatology of annual land surface temperature. *Remote Sens.* 7 (3), 2850–2870. <https://doi.org/10.3390/rs70302850>.
- Bechtel, B., Sismanidis, P., 2018. Time series analysis of moderate resolution land surface temperatures. In: Weng, Q. (Ed.), *Remote Sensing Time Series Image Processing*. CRC Press, pp. 111–142.
- Bechtel, B., Zakšek, K., Hoshyaripour, G., 2012. Downscaling land surface temperature in an urban area: a case study for Hamburg, Germany. *Remote Sens.* 4 (10), 3184–3200. <https://doi.org/10.3390/rs4103184>.
- Chow, W.T.L., Roth, M., 2006. Temporal dynamics of the urban heat island of Singapore. *Int. J. Climatol.* 26 (15), 2243–2260. <https://doi.org/10.1002/joc.1364>.
- Clinton, N., Gong, P., 2013. MODIS detected surface urban heat islands and sinks: global locations and controls. *Remote Sens. Environ.* 134 (5), 294–304. <https://doi.org/10.1016/j.rse.2013.03.008>.
- de Faria Peres, L., de Lucena, A.J., Rotunno Filho, O.C., de Almeida França, J.R., 2018. The urban heat island in Rio de Janeiro, Brazil, in the last 30 years using remote sensing data. *Int. J. Appl. Earth Obs. Geoinf.* 64, 104–116. <https://doi.org/10.1016/j.jag.2017.08.012>.
- Duan, S.B., Li, Z.L., Tang, B.H., Wu, H., Tang, R., 2014. Direct estimation of land-surface diurnal temperature cycle model parameters from MSG-SEVIRI brightness temperatures under clear sky conditions. *Remote Sens. Environ.* 150, 34–43. <https://doi.org/10.1016/j.rse.2014.04.017>.
- Fang, Y., Zhan, W., Huang, F., Gao, L., Quan, J., Zou, Z., 2017. Hourly variation of surface urban heat island over the Yangtze River Delta urban agglomeration. *Adv. Earth Science* 32 (2), 187–198.
- Flores, R.J.L., Pereira Filho, A.J., Karam, H.A., 2016. Estimation of long term low resolution surface urban heat island intensities for tropical cities using MODIS remote sensing data. *Urban Clim.* 17, 32–66.
- Gawuc, L., Struzewska, J., 2016. Impact of MODIS quality control on temporally aggregated urban surface temperature and long-term surface urban heat island intensity. *Remote Sens.* 8 (5), 374. <https://doi.org/10.3390/rs8050374>.
- Gong, P., Liang, S., Carlton, E.J., Jiang, Q., Wu, J., Wang, L., Remais, J.V., 2012. Urbanisation and health in China. *Lancet* 379 (9818), 843–852. [https://doi.org/10.1016/S0140-6736\(11\)61878-3](https://doi.org/10.1016/S0140-6736(11)61878-3).
- Göttsche, F.M., Olesen, F.S., 2009. Modelling the effect of optical thickness on diurnal cycles of land surface temperature. *Remote Sens. Environ.* 113 (11), 2306–2316.
- Haashemi, S., Weng, Q., Darvishi, A., Alavipanah, S., 2016. Seasonal variations of the surface urban heat island in a semi-arid city. *Remote Sens.* 8 (4), 352. <https://doi.org/10.3390/rs8040352>.
- He, B.J., 2018. Potentials of meteorological characteristics and synoptic conditions to mitigate urban heat island effects. *Urban Clim.* 24, 26–33.
- Hong, F., Zhan, W., Göttsche, F.M., Liu, Z., Zhou, J., Huang, F., Lai, J., Li, M., 2018. Comparison of four-parameter diurnal land surface temperature cycle under clear-sky using in-situ and satellite data. *ISPRS J. Photogramm. Remote Sens.* 142, 190–204.
- Hu, L., Brunsell, N.A., 2015. A new perspective to assess the urban heat island through remotely sensed atmospheric profiles. *Remote Sens. Environ.* 158, 393–406. <https://doi.org/10.1016/j.rse.2014.10.022>.
- Hu, L., Monaghan, A., Voogt, J.A., Barlage, M., 2016. A first satellite-based observational assessment of urban thermal anisotropy. *Remote Sens. Environ.* 181, 111–121. <https://doi.org/10.1016/j.rse.2016.03.043>.
- Huang, F., Zhan, W., Duan, S.B., Ju, W., Quan, J., 2014. A generic framework for

- modeling diurnal land surface temperatures with remotely sensed thermal observations under clear sky. *Remote Sens. Environ.* 150, 140–151. <https://doi.org/10.1016/j.rse.2014.04.022>.
- Huang, F., Zhan, W., Voogt, J., Hu, L., Wang, Z., Quan, J., Ju, W., Guo, Z., 2016. Temporal upscaling of surface urban heat island by incorporating an annual temperature cycle model: a tale of two cities. *Remote Sens. Environ.* 186, 1–12. <https://doi.org/10.1016/j.rse.2016.08.009>.
- Imhoff, M.L., Zhang, P., Wolfe, R.E., Bounoua, L., 2010. Remote sensing of the urban heat island effect across biomes in the continental USA. *Remote Sens. Environ.* 114 (3), 504–513. <https://doi.org/10.1016/j.rse.2009.10.008>.
- Jin, M., 2000. Interpolation of surface radiative temperature measured from polar orbiting satellites to a diurnal cycle: 2. Cloudy-pixel treatment. *J. Geophys. Res.-Atmos.* 105 (D3), 4061–4076. <https://doi.org/10.1029/1999JD901088>.
- Jin, M., Dickinson, R.E., 1999. Interpolation of surface radiative temperature measured from polar orbiting satellites to a diurnal cycle 1. Without clouds. *J. Geophys. Res.-Atmos.* 104, 4061–4076. <https://doi.org/10.1029/1998JD200005>.
- Kalnay, E., Cai, M., 2003. Impact of urbanization and land-use change on climate. *Nature* 423 (6939), 528–531. <https://doi.org/10.1038/nature01675>.
- Keramitsoglou, I., Kiranoudis, C.T., Ceriola, G., Weng, Q., Rajasekar, U., 2011. Identification and analysis of urban surface temperature patterns in Greater Athens, Greece, using MODIS imagery. *Remote Sens. Environ.* 115 (12), 3080–3090. <https://doi.org/10.1016/j.rse.2011.06.014>.
- Keramitsoglou, I., Kiranoudis, C.T., Weng, Q., 2013. Downscaling geostationary land surface temperature imagery for urban analysis. *IEEE Geosci. Remote Sens. Lett.* 10 (5), 1253–1257.
- Lagourde, J.P., Hénon, A., Kurz, B., Moreau, P., Irvine, M., Voogt, J., Mestayer, P., 2010. Modelling daytime thermal infrared directional anisotropy over Toulouse city centre. *Remote Sens. Environ.* 114 (1), 87–105. <https://doi.org/10.1016/j.rse.2009.08.012>.
- Lai, J., Zhan, W., Huang, F., Quan, J., Hu, L., Gao, L., Ju, W., 2018. Does quality control matter? Surface urban heat island intensity variations estimated by satellite-derived land surface temperature products. *ISPRS J. Photogramm. Remote Sens.* 139, 212–227.
- Lazzarini, M., Marpu, P.R., Ghedira, H., 2013. Temperature-land cover interactions: the inversion of urban heat island phenomenon in desert city areas. *Remote Sens. Environ.* 130 (4), 136–152. <https://doi.org/10.1016/j.rse.2012.11.007>.
- Li, J., Song, C., Cao, L., Zhu, F., Meng, X., Wu, J., 2011. Impacts of landscape structure on surface urban heat islands: a case study of Shanghai, China. *Remote Sens. Environ.* 115 (12), 3249–3263. <https://doi.org/10.1016/j.rse.2011.07.008>.
- Li, Y.Y., Zhang, H., Kainz, W., 2012. Monitoring patterns of urban heat islands of the fast-growing Shanghai Metropolis, China: using time-series of Landsat TM/ETM+ data. *Int. J. Appl. Earth Obs. Geoinf.* 19 (10), 127–138. <https://doi.org/10.1016/j.jag.2012.05.001>.
- Liu, W., Feddema, O.J., L, Hu, Zung, O.A., Brunsell, N., 2017. Seasonal and diurnal characteristics of land surface temperature and major explanatory factors in Harris County, Texas. *Sustainability* 9 (12), 2324. <https://doi.org/10.3390/su9122324>.
- Mathew, A., Khandelwal, S., Kaul, N., 2018. Analysis of diurnal surface temperature variations for the assessment of surface urban heat island effect over Indian cities. *Energ. Buildings* 159, 271–295. <https://doi.org/10.1016/j.enbuild.2017.10.062>.
- Meng, Q., Zhang, L., Sun, Z., Meng, F., Wang, L., Sun, Y., 2018. Characterizing spatial and temporal trends of surface urban heat island effect in an urban main built-up area: a 12-year case study in Beijing, China. *Remote Sens. Environ.* 204, 826–837. <https://doi.org/10.1016/j.rse.2017.09.019>.
- Nichol, J.E., 2005. Remote sensing of urban heat islands by day and night. *Photogramm. Eng. Remote. Sens.* 71 (5), 613–621. <https://doi.org/10.14358/PERS.71.5.613>.
- Nichol, J.E., To, P.H., 2012. Temporal characteristics of thermal satellite images for urban heat stress and heat island mapping. *ISPRS J. Photogramm. Remote Sens.* 74, 153–162. <https://doi.org/10.1016/j.isprsjprs.2012.09.007>.
- Oke, T.R., 1982. The energetic basis of the urban heat island. *Q. J. R. Meteorol. Soc.* 1–24. <https://doi.org/10.1002/qj.49710845502>.
- Oke, T.R., Mills, G., Christen, A., Voogt, J., 2017. *Urban climate*. Cambridge University Press.
- Patz, J.A., Campbell-Lendrum, D., Holloway, T., Foley, J.A., 2005. Impact of regional climate change on human health. *Nature* 438 (7066), 310.
- Peng, S., Piao, S., Ciais, P., Friedlingstein, P., Ottle, C., Breon, F.M., Nan, H., Zhou, L., Myneni, R.B., 2012. Surface urban heat island across 419 global big cities. *Environ. Sci. Technol.* 46 (2), 696–703. <https://doi.org/10.1021/es2030438>.
- Pichierri, M., Bonafoni, S., Biondi, R., 2012. Satellite air temperature estimation for monitoring the canopy layer heat island of Milan. *Remote Sens. Environ.* 127 (4), 130–138. <https://doi.org/10.1016/j.rse.2012.08.025>.
- Quan, J., Chen, Y., Zhan, W., Wang, J., Voogt, J., Wang, M., 2014. Multi-temporal trajectory of the urban heat island centroid in Beijing, China based on a Gaussian volume model. *Remote Sens. Environ.* 149 (7), 33–46. <https://doi.org/10.1016/j.rse.2014.03.037>.
- Ren, G.Y., Chu, Z.Y., Chen, Z.H., Ren, Y.Y., 2007. Implications of temporal change in urban heat island intensity observed at Beijing and Wuhan stations. *Geophys. Res. Lett.* 34 (5), 89–103. <https://doi.org/10.1029/2006GL027927>.
- Runnalls, K.E., Oke, T.R., 2000. Dynamics and controls of the near-surface heat island of Vancouver, British Columbia. *Phys. Geogr.* 21 (4), 283–304.
- Schädlich, S., Götsche, F.M., Olesen, F.S., 2001. Influence of land surface parameters and atmosphere on METEOSAT brightness temperatures and generation of land surface temperature maps by temporally and spatially interpolating atmospheric correction. *Remote Sens. Environ.* 75 (1), 39–46.
- Schwarz, N., Manceur, A.M., 2015. Analyzing the influence of urban forms on surface urban heat islands in Europe. *J. Urban Plann. Dev.* 141 (3), A4014003.
- Schwarz, N., Lautenbach, S., Seppelt, R., 2011. Exploring indicators for quantifying surface urban heat islands of European cities with MODIS land surface temperatures. *Remote Sens. Environ.* 115 (12), 3175–3186. <https://doi.org/10.1016/j.rse.2011.07.003>.
- Shastri, H., Barik, B., Ghosh, S., Venkataraman, C., Sadavarte, P., 2017. Flip flop of day-night and summer-winter surface urban heat island intensity in India. *Sci. Rep.* 7, 40178. <https://doi.org/10.1038/srep40178>.
- Shen, H., Huang, L., Zhang, L., Wu, P., Zeng, C., 2016. Long-term and fine-scale satellite monitoring of the urban heat island effect by the fusion of multi-temporal and multi-sensor remote sensed data: a 26-year case study of the city of Wuhan in China. *Remote Sens. Environ.* 172, 109–125. <https://doi.org/10.1016/j.rse.2015.11.005>.
- Sismanidis, P., Keramitsoglou, I., Kiranoudis, C.T., 2015a. A satellite-based system for continuous monitoring of surface urban heat islands. *Urban Clim.* 14, 141–153. <https://doi.org/10.1016/j.uclim.2015.06.001>.
- Sismanidis, P., Keramitsoglou, I., Kiranoudis, C.T., 2015b. Diurnal analysis of surface urban heat island using spatially enhanced satellite derived LST data. In: *Urban Remote Sens. Event*, pp. 1–4. <https://doi.org/10.1109/JURSE.2015.7120498>.
- Sobrino, J.A., Oltra-Carrío, R., Sòria, G., Bianchi, R., Paganini, M., 2012. Impact of spatial resolution and satellite overpass time on evaluation of the surface urban heat island effects. *Remote Sens. Environ.* 117, 50–56. <https://doi.org/10.1016/j.rse.2011.04.042>.
- Stathopoulou, M., Cartalis, C., 2009. Downscaling AVHRR land surface temperatures for improved surface urban heat island intensity estimation. *Remote Sens. Environ.* 113 (12), 2592–2605. <https://doi.org/10.1016/j.rse.2009.07.017>.
- Stewart, I.D., Oke, T.R., 2012. Local climate zones for urban temperature studies. *Bull. Am. Meteorol. Soc.* 93 (12), 1879–1900. <https://doi.org/10.1175/bams-d-11-00019.1>.
- Streutker, D.R., 2003. Satellite-measured growth of the urban heat island of Houston, Texas. *Remote Sens. Environ.* 85 (3), 282–289. [https://doi.org/10.1016/S0034-4257\(03\)00007-5](https://doi.org/10.1016/S0034-4257(03)00007-5).
- Tang, B., Bi, Y., Li, Z.A., Xia, J., 2008. Generalized split-window algorithm for estimate of land surface temperature from Chinese geostationary FengYun meteorological satellite (FY-2C) data. *Sensors* 8 (2), 933–951. <https://doi.org/10.3390/sensors8020933>.
- Tran, H., Uchihama, D., Ochi, S., Yasuoka, Y., 2006. Assessment with satellite data of the urban heat island effects in Asian mega cities. *Int. J. Appl. Earth Obs. Geoinf.* 8 (1), 34–48. <https://doi.org/10.1016/j.jag.2005.05.003>.
- Voogt, J.A., 2008. Assessment of an urban sensor view model for thermal anisotropy. *Remote Sens. Environ.* 112 (2), 482–495. <https://doi.org/10.1016/j.rse.2007.05.013>.
- Voogt, J.A., Oke, T.R., 2003. Thermal remote sensing of urban climates. *Remote Sens. Environ.* 86 (3), 370–384. [https://doi.org/10.1016/s0034-4257\(03\)00079-8](https://doi.org/10.1016/s0034-4257(03)00079-8).
- Wan, Z., 2008. New refinements and validation of the MODIS land-surface temperature/emissivity products. *Remote Sens. Environ.* 112 (1), 59–74. <https://doi.org/10.1016/j.rse.2006.06.026>.
- Wan, Z., Dozier, J., 1996. A generalized split-window algorithm for retrieving land-surface temperature from space. *IEEE Trans. Geosci. Remote Sens.* 34 (4), 892–905. <https://doi.org/10.1109/36.508406>.
- Wang, J., Huang, B., Fu, D., Atkinson, P., 2015. Spatiotemporal variation in surface urban heat island intensity and associated determinants across major Chinese cities. *Remote Sens.* 7 (4), 3670. <https://doi.org/10.3390/rs70403670>.
- Wang, K., Jiang, S., Wang, J., Zhou, C., Wang, X., Lee, X., 2017. Comparing the diurnal and seasonal variabilities of atmospheric and surface urban heat islands based on the Beijing urban meteorological network. *J. Geophys. Res.-Atmos.* 122 (4), 2131–2154. <https://doi.org/10.1002/2016JD025304>.
- Weng, Q., 2009. Thermal infrared remote sensing for urban climate and environmental studies: methods, applications, and trends. *ISPRS J. Photogramm. Remote Sens.* 64 (4), 335–344. <https://doi.org/10.1016/j.isprsjprs.2009.03.007>.
- Weng, Q., Rajasekar, U., Hu, X.F., 2011. Modeling urban heat islands and their relationship with impervious surface and vegetation abundance by using ASTER images. *IEEE Trans. Geosci. Remote Sens.* 49 (10), 4080–4089. <https://doi.org/10.1109/TGRS.2011.2128874>.
- Yuan, F., Bauer, M.E., 2007. Comparison of impervious surface area and normalized difference vegetation index as indicators of surface urban heat island effects in Landsat imagery. *Remote Sens. Environ.* 106 (3), 375–386. <https://doi.org/10.1016/j.rse.2006.09.003>.
- Zakšek, K., Oštir, K., 2012. Downscaling land surface temperature for urban heat island diurnal cycle analysis. *Remote Sens. Environ.* 117, 114–124. <https://doi.org/10.1016/j.rse.2011.05.027>.
- Zhan, W., Chen, Y., Voogt, J.A., Zhou, J., Wang, J., Ma, W., Liu, W., 2012. Assessment of thermal anisotropy on remote estimation of urban thermal inertia. *Remote Sens. Environ.* 123, 12–24. <https://doi.org/10.1016/j.rse.2012.03.001>.
- Zhan, W., Chen, Y., Zhou, J., Wang, J., Liu, W., Voogt, J.A., Zhu, X., Quan, J., Li, J., 2013. Disaggregation of remotely sensed land surface temperature: literature survey, taxonomy, issues, and caveats. *Remote Sens. Environ.* 131 (8), 119–139. <https://doi.org/10.1016/j.rse.2012.12.014>.
- Zhao, L., Lee, X., Smith, R.B., Oleson, K., 2014. Strong contributions of local background climate to urban heat islands. *Nature* 511 (7508), 216–219. <https://doi.org/10.1038/nature13462>.
- Zheng, J., Yin, Y., Li, B., 2010. A new scheme for climate regionalization in China. *Acta Geograph. Sin.* 65 (1), 3–13.
- Zhou, J., Li, J., Yue, J., 2010. Analysis of urban heat island (UHI) in the Beijing metropolitan area by time-series MODIS data. In: *IEEE International Geoscience and Remote Sensing Symposium (IGARSS 2010)*, pp. 3327–3330.
- Zhou, J., Chen, Y., Wang, J., Zhan, W., 2011. Maximum nighttime urban heat island (UHI) intensity simulation by integrating remotely sensed data and meteorological observations. *IEEE J. Sel. Top. Appl. Earth Obs. Remote Sens.* 4, 138–146. <https://doi.org/10.1109/jstars.2010.2070871>.
- Zhou, J., Chen, Y., Zhang, X., Zhan, W., 2013a. Modelling the diurnal variations of urban

- heat islands with multi-source satellite data. *Int. J. Remote Sens.* 34 (21), 7568–7588. <https://doi.org/10.1080/01431161.2013.821576>.
- Zhou, B., Rybski, D., Kropp, J.P., 2013b. On the statistics of urban heat island intensity. *Geophys. Res. Lett.* 40 (20), 5486–5491. <https://doi.org/10.1002/2013GL057320>.
- Zhou, D., Zhao, S., Liu, S., Zhang, L., Zhu, C., 2014. Surface urban heat island in China's 32 major cities: spatial patterns and drivers. *Remote Sens. Environ.* 152, 51–61. <https://doi.org/10.1016/j.rse.2014.05.017>.
- Zhou, B., Rybski, D., Kropp, J.P., 2017. The role of city size and urban form in the surface urban heat island. *Sci. Rep.* 7 (1), 4791. <https://doi.org/10.1038/s41598-017-04242-2>.